

## Spectroscopy of the Transition State: Hydrogen Abstraction Reactions of Fluorine

S. E. Bradforth, D. W. Arnold,<sup>†</sup> R. B. Metz,<sup>‡</sup> A. Weaver, and D. M. Neumark<sup>\*,§</sup>

Department of Chemistry, University of California, Berkeley, California 94720 (Received: February 21, 1991)

The reactions  $F + CH_3OH \rightarrow HF + CH_3O$ ,  $F + C_2H_5OH \rightarrow HF + C_2H_5O$ , and  $F + OH \rightarrow HF + O(^3P, ^1D)$  are studied by photoelectron spectroscopy of the negative ions  $CH_3OHF^-$ ,  $C_2H_5OHF^-$ , and  $OHF^-$ . In each case, photodetachment accesses the transition-state region for direct hydrogen abstraction. The photoelectron spectra exhibit resolved vibrational structure which is sensitive to details of the potential surface in the transition-state region. To aid in the interpretation of the spectra, ab initio equilibrium structures, harmonic frequencies, and hydrogen bond dissociation energies are calculated for the ions  $CH_3OHF^-$  and  $OHF^-$ . The anharmonic hydroxyl hydrogen stretching potential is also calculated for the two ions. Using the calculated ion properties and the fitted ab initio reaction surfaces of Sloan et al. (*J. Chem. Phys.* 1981, 75, 1190), a two-dimensional dynamical simulation of the photoelectron spectrum of  $OHF^-$  is presented and modifications to the reaction surfaces are discussed. The spectra of the alcohol complexes are discussed in light of this simulation, and the role of the "bath" degrees of freedom in these spectra is considered.

## Introduction

During the past several years, considerable progress has been made toward the spectroscopic characterization of the transition state in simple chemical reactions. An array of frequency<sup>1</sup> and time-resolved<sup>2</sup> techniques has been developed which allows one to directly probe the transition-state region of the potential energy surfaces describing these reactions. These experiments are aimed at achieving a better understanding of the microscopic forces that govern the dynamics of bimolecular and unimolecular reactions.

One of the more promising approaches to this problem has been to photodetach a stable negative ion in order to form an unstable neutral complex in the vicinity of the transition state for a chemical reaction. For example, in a study of a unimolecular transition state, Lineberger and co-workers<sup>3</sup> used photoelectron spectroscopy of  $C_2H_2^-$  to investigate the unstable vinylidene radical, which rapidly isomerizes to acetylene. In an experiment that serves as a precursor to the work described here, Brauman and co-workers<sup>4</sup> examined total photodetachment cross sections in the visible and near-ultraviolet ( $\lambda > 370$  nm) regions for several ions of the form  $ROHF^-$ , thereby learning about the relationship of the ion geometry to the potential energy surface for the  $F + ROH \rightarrow HF + RO$  reaction.

In our laboratory, negative ion photoelectron spectroscopy<sup>5-7</sup> and threshold photodetachment<sup>8</sup> are used to study the transition-state region of bimolecular hydrogen exchange reactions  $A + HB \rightarrow HA + B$ . By photodetaching the stable, hydrogen-bonded  $AHB^-$  anion, one can form an unstable  $[AHB]$  complex located near the transition state for the bimolecular reaction. Most of our work to date has been on triatomic systems where A and B are like<sup>5,6,8</sup> or unlike<sup>7</sup> halogen atoms. The photoelectron spectra of the  $AHB^-$  bihalide anions yield resolved vibrational structure characteristic of the unstable  $[AHB]$  complex. This structure is very sensitive to the nature of the  $A + HB$  potential energy surface near the transition state.

In this paper, the extension of our method to reactions involving polyatomic reactants is described. We report studies<sup>9</sup> of the reactions  $F + CH_3OH \rightarrow HF + CH_3O$  and  $F + C_2H_5OH \rightarrow HF + C_2H_5O$  via photoelectron spectroscopy of  $CH_3OHF^-$  and  $C_2H_5OHF^-$ . In both cases, the photoelectron spectra reveal resolved vibrational features attributable to the  $[ROHF]$  transition-state region ( $R = CH_3, C_2H_5$ ). We also report a study of the related, but simpler, triatomic reaction,  $F + OH \rightarrow HF + O$ , from the photoelectron spectrum of the radical anion  $OHF^-$ . The results on this last system are novel in their own right, but they also provide a model to compare and understand the structure manifested in the spectra of the polyatomic systems.

There is a substantial body of experimental and theoretical work in the literature on the hydrogen abstraction reactions of fluorine.

TABLE I: Hydrogen Abstraction Reactions of Fluorine

reaction	$\Delta H_{298}^0$ , <sup>a</sup> kcal/mol	$\Delta E_0^0$ , <sup>b</sup> kcal/mol	$k_{298}^0$ , <sup>c</sup> $10^{11}$ cm <sup>3</sup> s <sup>-1</sup>	$E_b$ , <sup>d</sup> kcal/mol
F + H-O <sup>e</sup>	-34.0	-34.0	4.1	
F + H-OCH <sub>3</sub>	-32.2	-32.6	7.7	
F + H-OC <sub>2</sub> H <sub>5</sub>	-32.0	-32.3	6.3	
F + H-H	-32.1	-32.1	2.5	~2
F + H-OH	-17.2	-17.5	1.4	4
F + H-CH <sub>2</sub> OH	-42.2	-42.9	1.7 <sup>f</sup>	
F + H-CH(CH <sub>3</sub> )OH and F + H-CH <sub>2</sub> CH <sub>2</sub> OH	-43.2	-43.9	1.4 <sup>f</sup>	

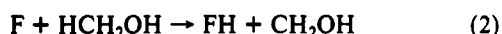
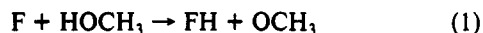
<sup>a</sup> Exothermicity,  $\Delta H_{298}^0$ , calculated from  $DH_{298}(H-X)$  for  $CH_3OH$  (ref 31),  $C_2H_5OH$  (ref 32),  $H_2O$  (ref 33), and  $H-CH_2OH$  and  $H-C-H(CH_3)OH$  (ref 34) and  $D_0^0$  for  $OH$ ,  $H_2$ , and  $HF$  (ref 37). <sup>b</sup> Exoergicity,  $\Delta E_0^0$ , calculated by correction to  $\Delta H_{298}^0$  using vibrational frequencies for  $CH_3OH$  and  $H_2O$  (ref 35) and  $CH_3O$  and  $CH_2OH$  (ref 36); vibrational corrections for ethanol reactions assumed equal to those of methanol. All molecules are assumed to be ideal gases, and both hindered and full rotations are treated classically. <sup>c</sup> Kinetic data collected from refs 12, 17, 22, and 72. <sup>d</sup> Estimated classical barriers from refs 69, 70, and 72. <sup>e</sup> Products  $O(^3P) + HF$ . <sup>f</sup> This is the measured rate divided by the number of available chemically equivalent hydrogen atoms for abstraction.

The  $F + CH_3OH$  and  $F + C_2H_5OH$  reactions have been the subject of both kinetics and product-state-resolved experiments. For  $F + CH_3OH$ , two channels are available:

- (1) Brooks, P. R. *Chem. Rev.* 1988, 88, 407. Arrowsmith, P.; Bartoszek, F. E.; Bly, S. H. P.; Carrington, T., Jr.; Charters, P. E.; Polanyi, J. C. *J. Chem. Phys.* 1980, 73, 5895. Grienseisen, H. P.; Xue-Jing, H.; Kompa, K. L. *Chem. Phys. Lett.* 1981, 82, 421. Imre, D. G.; Kinsey, J. L.; Field, R. W.; Katayama, D. H. *J. Phys. Chem.* 1982, 86, 2564. Buelow, S.; Radhakrishnan, G.; Catanzarite, J.; Wittig, C. *J. Chem. Phys.* 1985, 83, 444. Kleiber, P. D.; Lyrra, A. M.; Sando, K. M.; Zaffropoulos, V.; Stwalley, W. C. *J. Chem. Phys.* 1986, 85, 5493. Benz, A.; Morgner, H. *Mol. Phys.* 1986, 57, 319. Breckenridge, W. H.; Jouvot, C.; Soep, B. *J. Chem. Phys.* 1986, 84, 1443. Lao, K. Q.; Person, M. D.; Xayaribon, P.; Butler, L. J. *J. Chem. Phys.* 1990, 92, 823.
- (2) Bowman, R. M.; Dantus, M.; Zewail, A. H. *Chem. Phys. Lett.* 1989, 156, 131. Scherer, N. F.; Sipes, C.; Bernstein, R. B.; Zewail, A. H. *J. Chem. Phys.* 1990, 92, 5239. Dantus, M.; Bowman, R. M.; Zewail, A. H. *J. Chem. Phys.* 1989, 91, 7437. Glowina, J. H.; Misewich, J. A.; Sorokin, P. P. *J. Chem. Phys.* 1990, 92, 3335.
- (3) Ervin, K. M.; Ho, J.; Lineberger, W. C. *J. Chem. Phys.* 1989, 91, 5974.
- (4) Moylan, C. R.; Dodd, J. D.; Han, C.; Brauman, J. I. *J. Chem. Phys.* 1987, 86, 5350.
- (5) Metz, R. B.; Weaver, A.; Bradforth, S. E.; Kitsopoulos, T. N.; Neumark, D. M. *J. Phys. Chem.* 1990, 94, 1377.
- (6) Weaver, A.; Metz, R. B.; Bradforth, S. E.; Neumark, D. M. *J. Phys. Chem.* 1988, 92, 5558.
- (7) Bradforth, S. E.; Weaver, A.; Arnold, D. W.; Metz, R. B.; Neumark, D. M. *J. Chem. Phys.* 1990, 92, 7205.
- (8) Waller, I. M.; Kitsopoulos, T. N.; Neumark, D. M. *J. Phys. Chem.* 1990, 94, 2240.
- (9) A communication of the  $CH_3OHF^-$  photoelectron spectrum has been published: Bradforth, S. E.; Weaver, A.; Metz, R. B.; Neumark, D. M. *Advances in Laser Science - IV Proceedings of the 1988 International Laser Science Conference*; AIP Conference Proceedings 191; American Institute of Physics: New York, 1989; p 657.

\* To whom correspondence should be addressed.

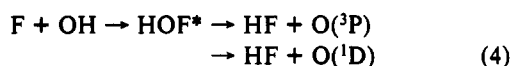
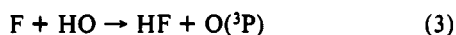
<sup>†</sup> NSF Predoctoral Fellow.<sup>‡</sup> University Fellow, University of California.<sup>§</sup> NSF Presidential Young Investigator and Alfred P. Sloan Fellow.



The exothermicities for these reactions are given in Table I. Both reactions 1 and 2 are very fast at room temperature:  $k_{\text{tot}} = 1 \times 10^{10}$ – $2 \times 10^{10} \text{ cm}^3 \text{ s}^{-1}$ .<sup>10–12</sup> There is a considerable range<sup>13,14</sup> of reported branching ratios.<sup>11–16</sup> However, there is a consensus that reaction 1 accounts for more than the statistical 25% of total product at room temperature, and this fraction may be as high as 80%.<sup>13</sup> For  $\text{F} + \text{C}_2\text{H}_5\text{OH}$ , there are three channels available. If the fluorine attack were completely non-site-specific, one would expect a branching ratio in  $\text{F} + \text{C}_2\text{H}_5\text{OH}$  of 18% for  $\text{C}_2\text{H}_5\text{O}$  formation. As with methanol, the reported branching ratios<sup>17,18</sup> indicate that fluorine abstracts at the hydroxyl group faster than at the methyl or methylene groups. Khatoon's work,<sup>12,17</sup> using isotopically labeled reactants and a mass spectrometric detection scheme, indicates that the probability of abstraction of a particular hydrogen by fluorine is 5 times more likely at the hydroxyl site than at one of the alkyl sites, for both methanol and ethanol. This preference in both reactions is interesting since the  $\text{CH}_3\text{O}$  and  $\text{C}_2\text{H}_5\text{O}$  product channels are less exoergic by 10 kcal/mol (see Table I). As we shall see, our experimental data addresses the dynamics of the hydroxyl hydrogen abstraction channel only.

The energy disposal in both products of reaction 1 can be measured: the HF product by infrared chemiluminescence and the  $\text{CH}_3\text{O}$  product by laser-induced fluorescence. This has been used in a series of experiments<sup>11,15,16,19</sup> to determine, in detail, how the partitioning of product energy compares to results for the well-characterized triatomic  $\text{F} + \text{HX}$  reactions ( $\text{X} = \text{halogen}$ ).<sup>20</sup> The results indicate that, for the  $\text{F} + \text{CH}_3\text{OH}$  reaction, the presence of a large number of product degrees of freedom has a small but noticeable effect on overall energy disposal, in comparison to the  $\text{F} + \text{HX}$  reactions. The fraction of available energy appearing as HF vibrational excitation is slightly less than in the  $\text{F} + \text{HX}$  reactions, and about 2% of the available energy appears as vibrational excitation of the  $\nu_3$  mode (C–O stretch) of the  $\text{CH}_3\text{O}$  radical. The single chemiluminescence study of  $\text{F} + \text{C}_2\text{H}_5\text{OH}$  suggests similar behavior for this system.<sup>21</sup> Thus, one expects the potential energy surfaces for both the  $\text{F} + \text{CH}_3\text{OH}$  and  $\text{F} + \text{C}_2\text{H}_5\text{OH}$  reactions to share important features with the  $\text{F} + \text{HX}$  surfaces, particularly a small entrance channel barrier to reaction.

The reaction of fluorine with hydroxyl has been less well studied. Possible reactions of F with OH are



In (3) and (5) fluorine directly attacks the hydrogen end of the

hydroxyl; (3) proceeds on a triplet surface and is exothermic by 34 kcal/mol, while (5), which is 11 kcal/mol endothermic, occurs on a singlet surface. This mechanism is akin to the reactions discussed so far with the alcohols. Reaction 4 involves the radical fluorine atom attacking the oxygen atom, the site of the unpaired electron on OH, and forming vibrationally hot  $\text{HOF}({}^1\text{A}')$ . This radical–radical recombination should proceed with no barrier. However, a spin-forbidden nonadiabatic transition is then required for  $\text{HF} + \text{O}({}^3\text{P})$  production. The overall room-temperature rate constant for reaction of  $\text{F} + \text{OH}$  by all pathways has been measured to be  $4.1 \times 10^{-11} \text{ cm}^3 \text{ s}^{-1}$ .<sup>22</sup>

Sloan and co-workers<sup>23</sup> have measured product-state distributions from the  $\text{F} + \text{OH}$  reaction. They observed infrared chemiluminescence from product HF vibrational levels up to  $v = 3$  when reacting F with  $\text{H}_2\text{O}$ . The  $\text{F} + \text{H}_2\text{O}$  reaction is exoergic enough to produce only  $\text{HF}(v = 0,1)$ . The observation of population in higher HF vibrational levels was explained in terms of a secondary reaction, of F with OH produced by the  $\text{F} + \text{H}_2\text{O}$  reaction, taking place in their chamber. The product vibrational and rotational distributions from the secondary reaction appeared to be statistical. On the basis of this and an ab initio calculation, which predicted a large barrier for (3), the authors concluded that the dominant reaction pathway is via attack of fluorine on the oxygen end of the OH molecule (4) and that HOF is a long-lived intermediate, which decays by a nonadiabatic transition. As we shall show below, the  $\text{OHF}^-$  photoelectron spectrum is quite sensitive to the barrier for direct abstraction (3), allowing us to test Sloan's conclusions. This adiabatic pathway for  $\text{F} + \text{OH}$  to yield  $\text{O}({}^3\text{P}) + \text{HF}$  by direct abstraction is entirely analogous to the alcohol reactions. Thus, we will also use the results on the  $\text{F} + \text{OH}$  system to serve as a model for understanding the  $\text{CH}_3\text{OHF}^-$  and  $\text{C}_2\text{H}_5\text{OHF}^-$  photoelectron spectra.

Our experiment starts with the negative ion analogue of the reaction transition state we wish to study. It is useful for that ion to be well-characterized. The  $\text{CH}_3\text{OHF}^-$  anion has been fairly well-studied and was first observed by Riveros in an ion cyclotron resonance (ICR) cell.<sup>24</sup> In this anion,  $\text{F}^-$  binds to the hydroxyl hydrogen of  $\text{CH}_3\text{OH}$ , since this hydrogen is considerably more acidic than the methyl hydrogens. Larson and McMahon determined the  $\text{CH}_3\text{OH} \cdot \text{F}^-$  binding energy to be 29.6 kcal/mol.<sup>25</sup> The proton affinity of  $\text{CH}_3\text{O}^-$  (or the gas-phase acidity of  $\text{CH}_3\text{OH}$ ) is slightly higher than that of  $\text{F}^-$  (381.2 versus 371.4 kcal/mol).<sup>26</sup> This means that  $\text{F}^- + \text{CH}_3\text{OH}$  is the lowest dissociation channel for  $\text{CH}_3\text{OHF}^-$ ; Jasinski et al.<sup>27</sup> have experimentally confirmed this by infrared multiphoton dissociation of the ion in an ICR cell. In addition, the relative proton affinities lead one to expect the shared proton in  $\text{CH}_3\text{OHF}^-$  to lie closer to the O atom than to the F atom in the ion equilibrium structure.

The proton affinity of  $\text{C}_2\text{H}_5\text{O}^-$  (378.1 kcal/mol)<sup>26</sup> is nearer to, but still higher than, that of  $\text{F}^-$ . Thus, it would be expected that the shared proton in  $\text{C}_2\text{H}_5\text{OHF}^-$ , though still closer to the O than the F atom, would be more evenly shared than in  $\text{CH}_3\text{OHF}^-$ . In agreement with this, the measured binding energy of  $\text{C}_2\text{H}_5\text{OHF}^-$ , 31.5 kcal/mol,<sup>25</sup> is higher than that of  $\text{CH}_3\text{OHF}^-$ . The  $\text{OHF}^-$  ion has not been observed previously, but since the proton affinity of  $\text{O}^-$  (382.2 kcal/mol)<sup>26</sup> is comparable to that of  $\text{CH}_3\text{O}^-$ , one expects binding and structure similar to that of the alcohol complexes, namely  $\text{OH} \cdot \text{F}^-$ .

The position of the shared proton in the anion is critical to our photoelectron spectroscopy experiment, since the region of the A + HB potential energy surface accessible via photodetachment

(10) Hoyermann, K.; Loftfield, N. L.; Sievert, R.; Wagner, H. G. *Symp. (Int.) Combust. [Proc.]*, 18th 1981, 831.

(11) Wickramaaratchi, M. A.; Setser, D. W.; Hildebrandt, H.; Körbitzer, B.; Heydtmann, H. *Chem. Phys.* 1985, 94, 109.

(12) Khatoon, T.; Hoyermann, K. *Ber. Bunsen-Ges. Phys. Chem.* 1988, 92, 669.

(13) McCauley, J. A.; Kelly, N.; Golde, M. F.; Kaufman, F. *J. Phys. Chem.* 1989, 93, 1014.

(14) Bogan, D. J.; Kaufman, M.; Hand, C. W.; Sanders, W. A.; Brauer, B. E. *J. Phys. Chem.* 1990, 94, 8128.

(15) MacDonald, R. G.; Sloan, J. J.; Wassell, P. T. *Chem. Phys.* 1979, 41, 201.

(16) Dill, B.; Heydtmann, H. *Chem. Phys.* 1980, 54, 9.

(17) Khatoon, T.; Edelbüttel-Einhaus, J.; Hoyermann, K.; Wagner, H. G. *Ber. Bunsen-Ges. Phys. Chem.* 1989, 93, 626.

(18) Meier, U.; Grotheer, H. H.; Riekert, G.; Just, Th. *Chem. Phys. Lett.* 1985, 115, 221.

(19) Agrawalla, B. S.; Setser, D. W. *J. Phys. Chem.* 1984, 88, 657.

(20) Jonathan, N.; Melliar-Smith, S.; Okuda, S.; Slater, D. H.; Timlin, D. *Mol. Phys.* 1971, 22, 561. Maylotte, D. H.; Polanyi, J. C.; Woodall, K. B. *J. Chem. Phys.* 1972, 57, 1547. Brandt, D.; Dickson, L. W.; Kwan, L. N. Y.; Polanyi, J. C. *Chem. Phys.* 1979, 39, 189. Tamagake, K.; Setser, D. W.; Sung, J. P. *J. Chem. Phys.* 1980, 73, 2203.

(21) Dill, B.; Hildebrandt, B.; Vanni, H.; Heydtmann, H. *Chem. Phys.* 1981, 58, 163.

(22) Walther, C.-D.; Wagner, H. G. *Ber. Bunsen-Ges. Phys. Chem.* 1983, 87, 403.

(23) Sloan, J. J.; Watson, D. G.; Williamson, J. M.; Wright, J. S. *J. Chem. Phys.* 1981, 75, 1190.

(24) Faigle, J. F. G.; Isolani, P. C.; Riveros, J. M. *J. Am. Chem. Soc.* 1976, 98, 2049.

(25) Larson, J. W.; McMahon, T. B. *J. Am. Chem. Soc.* 1983, 105, 2944.

(26) Lias, S. G.; Bartmess, J. E.; Liebman, J. F.; Holmes, J. L.; Levin, R. D.; Mallard, W. G. *J. Phys. Chem. Ref. Data* 1988, 17 (Suppl. 1), 666, 677, 768, 791.

(27) Jasinski, J. M.; Rosenfeld, R. N.; Meyer, F. K.; Brauman, J. I. *Chem. Phys. Lett.* 1982, 104, 652.

is determined by the ion geometry. For example, we have reported studies of the Br + HI, Cl + HI, and F + HI reactions by photoelectron spectroscopy of BrHI<sup>-</sup>, ClHI<sup>-</sup>, and FHI<sup>-</sup>.<sup>7</sup> The proton affinities of Br<sup>-</sup>, Cl<sup>-</sup>, and F<sup>-</sup> are at least 10 kcal/mol greater than that of I<sup>-</sup>. We therefore expect  $R_{HX} < R_{HI}$  in the XHI<sup>-</sup> anions. The ions consequently have better geometric overlap with the I + HX product valleys on their respective neutral potential energy surfaces, and this is indeed the region that is probed in the reported photoelectron spectra. This turns out to be the case for all the asymmetric X + HY reactions, where X and Y are halogen atoms.

On the other hand, photodetachment of CH<sub>3</sub>OHF<sup>-</sup>, C<sub>2</sub>H<sub>5</sub>OHF<sup>-</sup>, and OHF<sup>-</sup> should result in considerably better overlap with the F + CH<sub>3</sub>OH, F + C<sub>2</sub>H<sub>5</sub>OH, or F + OH reactant valleys, respectively. This is arguably the most important region of the surface since it includes the barrier along the minimum-energy path. Thus, the significance of the results presented here is twofold. The photoelectron spectra of the ROHF<sup>-</sup> and OHF<sup>-</sup> anions represent an extension of our "transition-state spectroscopy" method to more complex reactions. Furthermore, the spectra of all three systems allow us to probe a more interesting part of the potential energy surface for the corresponding neutral reaction in comparison to the XHY<sup>-</sup> spectra.

In addition to the experimental results, we present ab initio calculations that describe the equilibrium structure, harmonic frequencies, and binding energies of the CH<sub>3</sub>OHF<sup>-</sup> and OHF<sup>-</sup> ions. A two-dimensional dynamical simulation of the OHF<sup>-</sup> photoelectron spectrum is then described, which is used as a starting point for considering modifications to the F + OH reaction potential surfaces. The spectra of the polyatomic systems are discussed, with reference to the OHF<sup>-</sup> simulation, and finally the role of the extra degrees of freedom is evaluated.

### Experimental Section

The time-of-flight photoelectron spectrometer used in this study has been described in detail elsewhere.<sup>5</sup> Briefly, negative ions are formed by crossing the expansion of a pulsed molecular beam valve with a 1-keV continuous electron beam close to the valve orifice. For production of OHF<sup>-</sup>, the gas mixture expanded through the valve was N<sub>2</sub>O with a trace concentration of HF. The OHF<sup>-</sup> formation mechanism is probably via dissociative attachment of N<sub>2</sub>O by slow secondary electrons, N<sub>2</sub>O + e<sup>-</sup> → O<sup>-</sup> + N<sub>2</sub>, followed by the clustering process O<sup>-</sup> + HF + M → OHF<sup>-</sup> + M. The best way we found to make a stable beam of CH<sub>3</sub>OHF<sup>-</sup> (or C<sub>2</sub>H<sub>5</sub>OHF<sup>-</sup>) was to put a few drops of CH<sub>3</sub>OH (or C<sub>2</sub>H<sub>5</sub>OH) into the pulsed beam valve, which hangs vertically in the source chamber, and pass a 5% NF<sub>3</sub>/He mixture through the valve. Dissociative attachment to NF<sub>3</sub> produces F<sup>-</sup>, which then clusters to the alcohol. Under the same expansion conditions, we have obtained vibrational temperatures of 150–300 K for CH<sub>2</sub>CN<sup>-</sup> and rotational temperatures of less than 100 K for SH<sup>-</sup> prepared in a similar source.<sup>28</sup>

The ions formed in the source chamber are extracted perpendicular to the molecular beam and injected into a Wiley-McLaren type time-of-flight mass spectrometer.<sup>29</sup> Ions separate according to their masses, and the ion of interest is photodetached by the fifth harmonic of a pulsed Nd:YAG laser (213 nm, 5.825 eV). The photoelectrons produced by this process are ejected into all solid angles, and a small fraction (10<sup>-4</sup>) is collected by a detector at the end of a 1-m field-free flight tube. The flight time of the electrons is recorded and converted into center-of-mass kinetic energy. The energy resolution function of the instrument is given in ref 5; essentially the apparatus' electron energy resolution is 8 meV at 0.65 eV and degrades as E<sup>3/2</sup> at higher electron kinetic energies.

### Results and Analysis

**1. Experimental Results.** The CH<sub>3</sub>OHF<sup>-</sup> and C<sub>2</sub>H<sub>5</sub>OHF<sup>-</sup> photoelectron spectra are shown in Figure 1. The spectra are

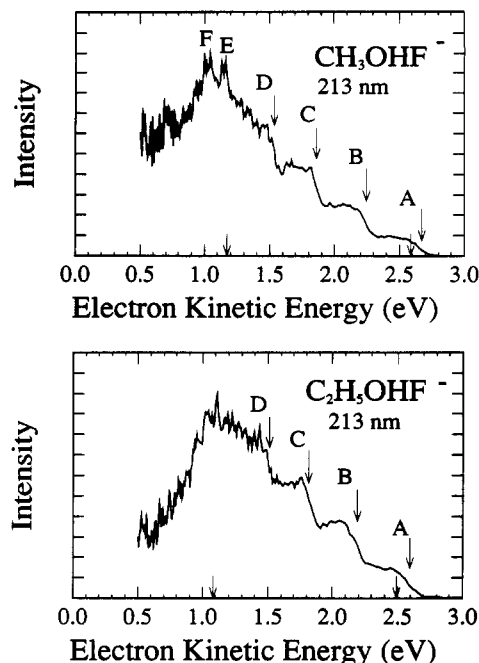


**Figure 1.** Photoelectron spectra of (a) CH<sub>3</sub>OHF<sup>-</sup> and (b) C<sub>2</sub>H<sub>5</sub>OHF<sup>-</sup> recorded at 213 nm. Arrows against axis indicate energies corresponding to product and reactant asymptotes (see text). Step onsets are indicated by arrows above spectrum.

considerably more complex than the spectra of the triatomic anions we have previously studied. The clearest structural pattern in both spectra are the four regularly spaced steps between 1.2 and 2.8 eV. The labeled arrows (A–D), at 2.69, 2.24, 1.85, and 1.54 eV in Figure 1a and 2.58, 2.18, 1.83, and 1.50 eV in Figure 1b, mark the onset of each step. There are two sharper features, E at 1.15 eV, and F at 1.03 eV, in the CH<sub>3</sub>OHF<sup>-</sup> spectrum.

The peaks are labeled in order of increasing internal energy of the neutral complex. The electron kinetic energies (eKEs) are related to the internal energies of the neutral species ( $E_i^{(0)}$ ) by

$$eKE = h\nu - D_0^0(\text{ROHF}^-) - EA(\text{F}) - \Delta E_0^0 - E_i^{(0)} + E_i^{(-)} \quad (6)$$

Thus, peaks with highest electron kinetic energy correspond to neutral states with lowest internal energy. In (6),  $h\nu$  is the laser photon energy, 5.825 eV,  $EA(\text{F})$  is the electron affinity of fluorine, 3.399 eV,<sup>30</sup> and  $D_0^0(\text{ROHF}^-)$  is the bond dissociation energy of ground-state ROHF<sup>-</sup> to form ground-state ROH and F<sup>-</sup>. For  $D_0^0(\text{CH}_3\text{OHF}^-)$ , we use the experimental<sup>25</sup> bond dissociation enthalpy,  $\Delta H_{298}$ , and correct to 0 K using a set of ab initio calculated frequencies (see below); this yields 1.244 eV. For  $D_0^0(\text{C}_2\text{H}_5\text{OHF}^-)$ , we use the experimental<sup>25</sup> bond enthalpy for this ion, and the same correction to 0 K as calculated for CH<sub>3</sub>OHF<sup>-</sup>, yielding 1.327 eV.  $\Delta E_0^0$  is the exoergicity for the reaction F + ROH → RO + HF and is given in Table I.<sup>31–36</sup>  $E_i^{(0)}$  is the energy of the [ROHF] complex relative to ground-state RO + HF.  $E_i^{(-)}$  is the internal energy of the precursor ion ROHF<sup>-</sup> above zero point. As all the anions studied here are expected to be prepared cold, this quantity is assumed throughout to be zero.

The eKE corresponding to  $E_i^{(0)} = 0$  is shown by arrows against the axis at 2.60 eV (Figure 1a) and 2.50 eV (Figure 1b). These

(30) Hotop, H.; Lineberger, W. C. *J. Chem. Phys. Ref. Data* **1985**, *14*, 731.

(31) Batt, L.; McCulloch, R. D. *Int. J. Chem. Kinet.* **1976**, *8*, 491.

(32) Batt, L.; Christie, K.; Milne, R. T.; Summers, A. J. *Int. J. Chem. Kinet.* **1974**, *6*, 877.

(33) Kerr, J. A. *Chem. Rev.* **1966**, *66*, 465.

(34) McMillen, D. F.; Golden, D. M. *Annu. Rev. Phys. Chem.* **1982**, *33*, 493.

(35) Shimanouchi, T. *Tables of Molecular Vibrational Frequencies*, Consolidated Vol. I; *Natl. Stand. Ref. Data Ser. (U.S., Natl. Bur. Stand.)* **1979**, NSRDS-NBS 39.

(36) Jacox, M. E. *J. Chem. Phys. Ref. Data* **1988**, *17*, 269.

(28) Kitsopoulos, T. N.; Waller, I. M.; Loeser, J. G.; Neumark, D. M. *Chem. Phys. Lett.* **1989**, *159*, 300.

(29) Wiley, W. C.; McLaren, I. H. *Rev. Sci. Instrum.* **1955**, *26*, 1150.

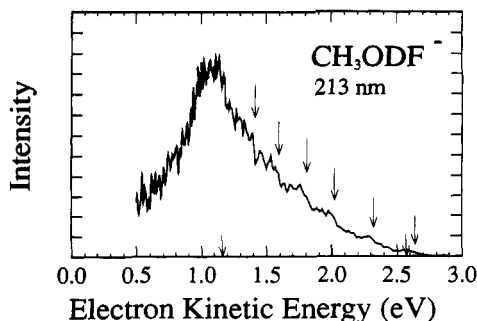


Figure 2. Photoelectron spectrum of  $\text{CH}_3\text{ODF}^-$  recorded at 213 nm. Arrows as for Figure 1.

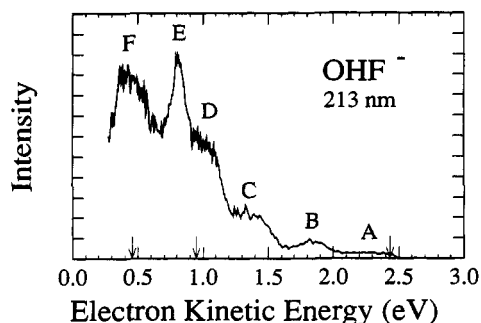


Figure 3. Photoelectron spectrum of  $\text{OHF}^-$  recorded at 213 nm. Arrows against the axis indicate energies corresponding to asymptotes for formation of  $\text{O}(^3\text{P}) + \text{HF}$ ,  $\text{F} + \text{OH}$ , and  $\text{O}(^1\text{D}) + \text{HF}$ , in order of decreasing electron kinetic energy.

arrows indicate the electron kinetic energy corresponding to photodetaching ground-state  $\text{CH}_3\text{OHF}^-$  ( $\text{C}_2\text{H}_5\text{OHF}^-$ ) and forming ground-state  $\text{HF} + \text{CH}_3\text{O}$  ( $\text{C}_2\text{H}_5\text{O}$ ). We refer to these energies henceforth as product asymptotes. The reactant asymptotes, indicated by arrows at 1.18 eV (Figure 1a) and 1.10 eV (Figure 1b), correspond to ground-state  $\text{F} + \text{CH}_3\text{OH}$  ( $\text{C}_2\text{H}_5\text{OH}$ ) formation for which  $E_i^{(0)} = -\Delta E_0^0$ . All the structure in each spectrum occurs at lower eKE than the product asymptote and is therefore due to states of the neutral complex that can dissociate to  $\text{HF} + \text{CH}_3\text{O}$  ( $\text{C}_2\text{H}_5\text{O}$ ) products. In addition, features in the spectra at lower eKE than the reactant asymptotes correspond to states of the complex that can also dissociate to  $\text{F} + \text{CH}_3\text{OH}$  ( $\text{C}_2\text{H}_5\text{OH}$ ) reactants.

The photoelectron spectrum of  $\text{CH}_3\text{ODF}^-$  (Figure 2) shows a clear isotope effect. The spectrum shows six steps more closely spaced than those in the  $\text{CH}_3\text{OHF}^-$  spectrum. This isotope effect suggests that the step structure is due to a vibrational mode of the neutral complex analogous to the  $\nu_3$  mode seen in the triatomic bihalide spectra;<sup>3-7</sup> that is, the light hydrogen atom is vibrating between the much heavier F atom and RO group in the complex. The spacing between the steps in Figure 1a,b is less than that between the first few vibrational levels of  $\text{HF}$ ,<sup>37</sup> and the spacing between the second, third, and fourth steps is less than the corresponding levels of the OH stretch in  $\text{CH}_3\text{OH}$ . This "red shift" occurs because the experiment probes the transition-state region where the reacting species are interacting strongly;<sup>5,6</sup> the H atom vibrates in a shallower potential than in isolated  $\text{HF}$  or  $\text{CH}_3\text{OH}$ .

The intensity in the  $\text{CH}_3\text{OHF}^-$  spectrum builds as one moves from the  $\text{HF} + \text{CH}_3\text{O}$  product asymptote to the  $\text{F} + \text{CH}_3\text{OH}$  reactant asymptote at lower electron kinetic energy. The intensity distribution in the  $\text{C}_2\text{H}_5\text{OHF}^-$  spectrum is similar, although there is relatively more signal near the  $\text{HF} + \text{C}_2\text{H}_5\text{O}$  asymptote. The breadth of all the features in the photoelectron spectra is considerably larger than the experimental resolution. Spectra recorded at 266 nm (4.66 eV, not shown) show the right-most steps in each

TABLE II: Estimated Peak Centers and Widths from the Photoelectron Spectra of  $\text{OHF}^-$ <sup>a</sup>

peak	electron kinetic energy		
	onset <sup>b</sup>	center <sup>c</sup>	width <sup>c</sup>
A	2.46 (0.01)	2.25 (0.02)	0.35 (0.03)
B	1.95 (0.02)	1.82 (0.02)	0.31 (0.03)
C	1.51 (0.02)	1.38 (0.04)	0.30 (0.04)
D	1.16 (0.02)	1.01 (0.02)	0.30 (0.04)
E		0.80 (0.01)	0.15 (0.03)
F		0.45 (0.03)	~0.4

<sup>a</sup> Onsets of four highest energy steps are also given. All energies in eV; approximate uncertainties shown in parentheses. <sup>b</sup> Step onsets are measured at 50% of rising edge. <sup>c</sup> Centers and widths are estimated by a six-Gaussian fit to the photoelectron spectrum. Because bands overlap, the estimated uncertainties are large.

of the 213-nm spectra with lower electron kinetic energy and therefore higher resolution. Despite this higher resolution, there is no additional structure observed; the step profiles are unchanged.

The photoelectron spectrum of  $\text{OHF}^-$  is shown in Figure 3. The peak positions and widths are listed in Table II. The electron kinetic energies corresponding to the dissociation asymptotes  $\text{O}(^3\text{P}) + \text{HF}$  (2.43 eV),  $\text{F}(^2\text{P}_{3/2}) + \text{OH}(^2\Pi_{3/2})$  (0.95 eV), and  $\text{O}(^1\text{D}) + \text{HF}$  (0.46 eV) are shown in Figure 3, as before, with arrows against the energy axis. These energies are calculated from a relationship similar to eq 6, along with our best ab initio ion binding energy estimate (see below), the exoergicity for reaction 3 in Table I, and the experimental<sup>38</sup> oxygen atomic energy level splittings. Again, all structure observed in the spectrum corresponds to states of the neutral unstable with respect to dissociation to the lowest energy product channel ( $\text{O}(^3\text{P}) + \text{HF}$ ). Moreover, peaks A–D correspond to neutral states which can only dissociate to  $\text{O}(^3\text{P}) + \text{HF}$  products.

The overall appearance of the  $\text{OHF}^-$  spectrum is clearly very similar to both of the  $\text{ROHF}^-$  spectra. This is an interesting result considering the far fewer vibrational degrees of freedom in the  $[\text{OHF}]$  complex as well as its different electronic character (see below). However, there are several differences between the  $\text{OHF}^-$  and  $\text{ROHF}^-$  spectra. The onset of structure occurs at almost 0.3 eV lower electron kinetic energy in the  $\text{OHF}^-$  spectrum. Between the product and reactant asymptotes, the  $\text{OHF}^-$  spectrum looks more like a set of broad peaks, in contrast to the step structure seen in the  $\text{CH}_3\text{OHF}^-$  and  $\text{C}_2\text{H}_5\text{OHF}^-$  spectra. The feature below the reactant asymptote in the  $\text{OHF}^-$  spectrum (labeled E) is much more distinct than any corresponding structure in the other spectra. Finally, the intensity in the  $\text{OHF}^-$  spectrum builds in the same way as the other spectra, but in this spectrum, there is even less intensity at the  $\text{O} + \text{HF}$  product asymptote than at the product asymptote in the  $\text{CH}_3\text{OHF}^-$  spectrum.

The photoelectron spectra of  $\text{OHF}^-$ ,  $\text{CH}_3\text{OHF}^-$ , and  $\text{C}_2\text{H}_5\text{OHF}^-$  all show maximum intensity near the asymptote for dissociation into reactants  $\text{F} + \text{OH}$ ,  $\text{F} + \text{CH}_3\text{OH}$ , and  $\text{F} + \text{C}_2\text{H}_5\text{OH}$  rather than the energetically lower product asymptote. This is in sharp contrast to the asymmetric bihalide ions,<sup>7</sup> all of which show maximum intensity at the product asymptote. We can understand the intensity distributions in terms of the qualitative discussion of the ion geometries in the Introduction. Because the proton affinities of  $\text{O}^-$ ,  $\text{CH}_3\text{O}^-$ , and  $\text{C}_2\text{H}_5\text{O}^-$  are 0.47, 0.42, and 0.29 eV higher than that of  $\text{F}^-$ , the hydrogen should lie closer to the O atom than the F atom in all three anions. We therefore expect good Franck–Condon overlap with  $\text{OH}\cdots\text{F}$  or  $\text{ROH}\cdots\text{F}$  configurations of the neutral complex localized in the entrance valley of the reactive potential energy surface. The overall intensity envelopes seen in the spectra are in accord with this reasoning. In particular, the observation that the  $\text{C}_2\text{H}_5\text{OHF}^-$  spectrum has more intensity at the product asymptote than the  $\text{CH}_3\text{OHF}^-$  spectrum is consistent with the higher proton affinity of  $\text{CH}_3\text{O}^-$ .

It is clear from this discussion that the anion geometry has a significant effect on the photoelectron spectrum. In contrast to

(37) Huber, K. P.; Herzberg, G. *Molecular Spectra and Molecular Structure IV. Constants of Diatomic Molecules*; Van Nostrand: New York, 1979.

(38) Moore, C. E. *Atomic Energy Levels*, Vol. I; *Natl. Stand. Ref. Data Ser. (U.S., Natl. Bur. Stand.)* 1971, NSRDS-NBS 35.

**TABLE III: Ab Initio Geometries and Zero-Point Energies for CH<sub>3</sub>OHF<sup>-</sup> and CH<sub>3</sub>OH<sup>a</sup>**

	CH <sub>3</sub> OHF <sup>-</sup>		CH <sub>3</sub> OH	
	RHF/ 6-31++G**	RMP2/ 6-31++G**	RHF/ 6-31++G**	RMP2/ 6-31++G**
<i>r</i> <sub>e</sub> (O-H)	1.004	1.059	0.942	0.964
<i>r</i> <sub>e</sub> (H-F)	1.462	1.373		
∠OHF	173.8	175.3		
<i>r</i> <sub>e</sub> (C-O)	1.376	1.399	1.401	1.427
∠COH	108.4	106.4	110.5	108.6
<i>r</i> <sub>e</sub> (C-H <sub>1r</sub> )	1.092	1.095	1.081	1.085
<i>r</i> <sub>e</sub> (C-H <sub>2</sub> )	1.094	1.099	1.087	1.091
∠OCH <sub>1r</sub>	109.4	109.3	107.1	106.2
∠H <sub>1r</sub> CH <sub>2</sub>	107.5	107.6	108.6	108.9
∠H <sub>2</sub> CH <sub>2</sub>	107.0	106.8	109.0	109.3
zpe, eV	1.513	1.426	1.496	1.434

<sup>a</sup> Bond lengths are in angstroms and bond angles in degrees.

**TABLE IV: Harmonic Frequencies (in cm<sup>-1</sup>), Calculated with 6-31++G\*\* Basis Set, for CH<sub>3</sub>OHF<sup>-</sup>**

mode	RHF	RMP2	mode	RHF	RMP2
ω <sub>1</sub> (a')	3133	3102	ω <sub>9</sub> (a')	333	391
ω <sub>2</sub> (a')	3106	3016	ω <sub>10</sub> (a')	168	167
ω <sub>3</sub> (a')	2901	2215	ω <sub>11</sub> (a'')	3115	3060
ω <sub>4</sub> (a')	1731	1649	ω <sub>12</sub> (a'')	1610	1526
ω <sub>5</sub> (a')	1634	1556	ω <sub>13</sub> (a'')	1282	1248
ω <sub>6</sub> (a')	1600	1498	ω <sub>14</sub> (a'')	1214	1189
ω <sub>7</sub> (a')	1253	1178	ω <sub>15</sub> (a'')	94	77
ω <sub>8</sub> (a')	1230	1132			

the bialide ions, no spectroscopic data exist for ROHF<sup>-</sup> and OHF<sup>-</sup>. Therefore, in order to obtain a more quantitative picture of the anions, we have performed ab initio calculations on OHF<sup>-</sup> and CH<sub>3</sub>OHF<sup>-</sup> to determine their structure and properties.

**2. Ab Initio Calculations: Method and Results.** Fully optimized geometries, frequencies, and dissociation energies were calculated for the hydrogen-bonded anions OHF<sup>-</sup> and CH<sub>3</sub>OHF<sup>-</sup> at both the Hartree-Fock (HF) and second-order Møller-Plesset (MP2) level of theory. In addition, MP4 level calculations were employed to estimate hydrogen bond dissociation energies. The calculations reported here were performed with the GAUSSIAN 86,<sup>39</sup> GAUSSIAN 88,<sup>40</sup> and CADPAC<sup>41</sup> ab initio packages available at the San Diego Supercomputing Center. The standard 6-31++G\*\* basis set was used throughout; the incorporation of diffuse functions (++) is mandatory for a proper description of these anions. For OHF<sup>-</sup>, a spin-unrestricted wave function was used to describe both the <sup>2</sup>Π ground and <sup>2</sup>Σ excited states.

The results of these calculations are summarized in Tables III-VII. For the purposes of analyzing our photoelectron spectra, the most important results are the ion equilibrium geometries, the shape of their potential surfaces along the hydroxyl hydrogen stretching coordinate, and the ab initio estimate of their dissociation energy into F<sup>-</sup> and OH or CH<sub>3</sub>OH. For the last of these, an estimate of the zero-point energy correction is required, so frequencies were calculated for the hydrogen-bonded ions and the product fragments at both the HF and MP2 level of theory. All energies quoted (*E*<sub>0</sub>) include this zero-point energy correction, which is applied at the same level of theory as the calculated energy (except for the MP4 energies where the MP2 zero-point energies are used). MP4 electronic energies include all single, double, triple, and quadruple excitations while maintaining a frozen core

(MP4SDTQ-FC); the MP2 energies have all electrons considered for correlation (MP2-FULL). The calculation of the ion force field, apart from providing zero-point energies, was also useful for (a) obtaining a reasonable form for each anion's vibrational normal coordinates and (b) providing an estimate for the hydrogen bond stretching frequencies in the ions. Both of these will be used in the dynamical calculations described below.

The dissociation fragments of OHF<sup>-</sup> and CH<sub>3</sub>OHF<sup>-</sup> that we need to consider are F<sup>-</sup>, CH<sub>3</sub>OH, CH<sub>3</sub>O<sup>-</sup>, HF, OH, and O<sup>-</sup>. Computations of fully optimized geometries and frequencies for these fragments compare well with literature values for calculations using similar sized basis sets. The MP2 geometries and frequencies agree well with experimental values for CH<sub>3</sub>OH, HF, and OH, and the fluorine electron affinity is well reproduced at the MP2 level. The oxygen electron affinity, calculated at the same level of theory, 1.09 eV, is in poorer agreement with the experimental value of 1.46 eV.<sup>30</sup> By calculating the MP2/6-31++G\*\* equilibrium geometry of the Jahn-Teller distorted ground state of CH<sub>3</sub>O,<sup>42</sup> and using scaled<sup>43</sup> harmonic frequencies from the HF/6-31++G\*\* force fields for ion and neutral, we computed a zero-point-corrected adiabatic electron affinity of 1.47 eV for CH<sub>3</sub>O. This is to be compared with the experimental value of 1.57 eV.<sup>44</sup>

**Geometries and Frequencies.** Our qualitative expectations for the hydrogen-bonded ion geometries and dissociation energies are based on the proton affinity scale and have been outlined above. We expect that the closer the proton affinity of the bases A<sup>-</sup> and B<sup>-</sup>, the larger the degree of sharing of the proton and the stronger the hydrogen bond in AHB<sup>-</sup>.<sup>25</sup> From comparison of the proton affinities of the methoxide, hydroxide, and fluoride ions, we expect the hydrogen to be closer to the oxygen than fluorine in both CH<sub>3</sub>OHF<sup>-</sup> and OHF<sup>-</sup>. The quantitative ab initio results shown in Tables III and VI show that indeed the hydrogen sits closer to the oxygen than the fluorine atom for both ions. In fact, the equilibrium parameters for the two ions are very similar; the difference in O-F separation is smaller than 0.01 Å, and the hydrogen position is different by only 0.02 Å. However, the ab initio calculations suggest that OHF<sup>-</sup> has the hydrogen more centrally located. This last result is contrary to the proton affinity argument, but CH<sub>3</sub>OH is only slightly more acidic than OH.

The equilibrium geometry for CH<sub>3</sub>OHF<sup>-</sup>, which has C<sub>s</sub> symmetry, is shown in Figure 4. The F<sup>-</sup>·H-CH<sub>2</sub>OH isomer is expected to lie considerably higher in energy than CH<sub>3</sub>OH·F<sup>-</sup>. The hydrogen bond is slightly bent, as found for F<sup>-</sup>(H<sub>2</sub>O),<sup>45</sup> because of a weak interaction with the other nearby hydrogen atoms. With regard to the methanol frame, the staggered conformer is preferred to minimize steric repulsion, but the barrier to internal rotation about the C-O bond is calculated to be even smaller than in methanol.<sup>46</sup> The equilibrium configuration was found by optimization of all geometric parameters; in particular, the methoxy frame was also allowed to relax in response to the perturbation by the F<sup>-</sup>. The changes in the frame with respect to the equilibrium CH<sub>3</sub>OH geometry described by the same theoretical model are modest (Table III). The principal differences are a contraction in *r*<sub>e</sub>(C-O) by 0.03 Å in CH<sub>3</sub>OHF<sup>-</sup> and some distortion of the bond angles around the tetrahedral carbon center. By comparison, the change at the active center is much larger: there is a 0.10-Å lengthening of the O-H bond in the ion at the MP2 level. The framework relaxation will be considered when discussing possible "bath" mode excitations in the CH<sub>3</sub>OHF<sup>-</sup> photoelectron spectra. Previous calculations<sup>47</sup> for this ion are in

(39) Frisch, M. J.; Binkley, J. S.; Schlegel, H. B.; Raghavachari, K.; Melius, C. F.; Martin, R. L.; Stewart, J. J. P.; Bobrowicz, F. W.; Rohlfing, C. M.; Kahn, L. R.; Defrees, D. J.; Seeger, R.; Whiteside, R. A.; Fox, D. J.; Fluder, E. M.; Pople, J. A. *GAUSSIAN 86*; Carnegie-Mellon Quantum Chemistry Publishing Unit: Pittsburgh, PA, 1984.

(40) Frisch, M. J.; Head-Gordon, M.; Schlegel, H. B.; Raghavachari, K.; Binkley, J. S.; Gonzalez, C.; Defrees, D. J.; Fox, D. J.; Whiteside, R. A.; Seeger, R.; Melius, C. F.; Baker, J.; Martin, R. L.; Kahn, L. R.; Stewart, J. J. P.; Fluder, E. M.; Topiol, S.; Pople, J. A. *GAUSSIAN 88*; Gaussian Inc.: Pittsburgh, PA, 1988.

(41) Amos, R. D.; Rice, J. E. *Cambridge Analytic Derivatives Package*; Cambridge, 1987.

(42) *r*<sub>e</sub>(C-H<sub>1r</sub>) = 1.096 Å, *r*<sub>e</sub>(C-H<sub>2</sub>) = 1.090 Å, *r*<sub>e</sub>(C-O) = 1.388 Å, ∠OCH<sub>1r</sub> = 104.6°, ∠OCH<sub>2</sub> = 112.1°, ∠H<sub>1r</sub>CH<sub>2</sub> = 108.1°. For a discussion of CH<sub>3</sub>O electronic structure calculations, see: Saebø, S.; Radom, L.; Schaefer, H. F. *J. Chem. Phys.* **1983**, *78*, 845.

(43) 0.9 times the Hartree-Fock harmonic frequency.

(44) Engelking, P. C.; Ellison, G. B.; Lineberger, W. C. *J. Chem. Phys.* **1978**, *69*, 1826.

(45) Yates, B. Y.; Schaefer, H. F.; Lee, T. J.; Rice, J. E. *J. Am. Chem. Soc.* **1988**, *110*, 6327.

(46) The difference between staggered and eclipsed at the RHF/6-31++G\*\* level for CH<sub>3</sub>OHF<sup>-</sup> is 165 cm<sup>-1</sup>, compared to 402 cm<sup>-1</sup> for CH<sub>3</sub>OH (this work).

TABLE V: Ab Initio Energies for CH<sub>3</sub>OHF<sup>-</sup>, Including Zero-Point Energies

$E_0$ total energy <sup>a</sup>	RHF/6-31++G**// RHF/6-31++G** <sup>b</sup>		RMP2/6-31++G**// RMP2/6-31++G**		RMP4/6-31++G**// RMP2/6-31++G** <sup>c</sup>	
	au	eV	au	eV	au	eV
CH <sub>3</sub> OHF <sup>-</sup> equilibrium	-214.45671	0.000	-215.02240	0.000	-215.04730	0.000
F <sup>-</sup> + HOCH <sub>3</sub> separated fragments	-214.41611	1.104	-214.97545	1.278	-215.00124	1.253
CH <sub>3</sub> O <sup>-</sup> + HF separated fragments	-214.39208	1.758	-214.95104	1.941	-215.97621	1.934

<sup>a</sup> Zero-point energies calculated from force field evaluated at same level of theory as energy, except MP4 where MP2 zero-point energies are used.

<sup>b</sup> Notation "a/b" means energy evaluated with theoretical model a at the optimized geometry calculated with model b. <sup>c</sup> RMP4(SDTQ) frozen core energies.

TABLE VI: Ab Initio Geometry and Frequencies for OHF<sup>-</sup>

method	$R_e(\text{O-H})$ , <sup>a</sup> Å	$R_e(\text{H-F})$ , Å	∠OHF	freq, cm <sup>-1</sup>	( $S^2$ )
UHF/6-31++G**	1.031	1.400	180.0	379, (1070, 1227), 2514	0.756
UMP2/6-31++G**	1.078	1.346	180.0	433, (1064, 1225), 2015	0.752

<sup>a</sup>  $R_e(\text{O-H})$  in the free hydroxyl radical is 0.955 Å (UHF/6-31++G\*\*), 0.973 Å (UMP2/6-31++G\*\*), and 0.970 Å (experimental, ref 37).

TABLE VII: Ab Initio Energies for OHF<sup>-</sup>, Including Zero-Point Energies

$E_0$ total energy <sup>a</sup>	UHF/6-31++G**// UHF/6-31++G**		UMP2/6-31++G**// UMP2/6-31++G**		UMP4/6-31++G**// UMP2/6-31++G** <sup>b</sup>	
	au	eV	au	eV	au	eV
OHF <sup>-</sup> equilibrium	-174.84998	0.000	-175.21214	0.000	-175.22800	0.000
F <sup>-</sup> + HO( <sup>2</sup> P) separated fragments	-174.80273	1.286	-175.16113	1.388	-175.17375	1.476
O( <sup>2</sup> P) + HF separated fragments	-174.78075	1.884	-175.13652	2.058	-115.15280	2.046

<sup>a</sup> Zero-point energies calculated from force field evaluated at same level of theory as energy, except for MP4 where MP2 zero-point energies used.

<sup>b</sup> UMP4(SDTQ) frozen core energies.

qualitative agreement with those shown here, but the earlier treatments were limited to small basis sets without a complete set of diffuse functions and neglected electron correlation.

For AHB<sup>-</sup> species, a pertinent question to ask is whether there are two minima on the potential energy surface, corresponding to AH<sup>-</sup>·B<sup>-</sup> and A<sup>-</sup>·HB, or whether the two coalesce to form one broad, fairly flat-bottomed minimum. In the case of the *symmetric* bihalide ions of AHA<sup>-</sup>, this is extremely important as it determines whether the equilibrium structure is centrosymmetric or not. For example, calculations<sup>48-50</sup> on ClHC<sup>-</sup> and BrHBr<sup>-</sup> show that a Hartree-Fock description predicts a double-minimum potential for these anions, whereas the inclusion of other electronic configurations in the ground-state wave function leads to a significant lowering of the energy for centrosymmetric geometries compared to the AH<sup>-</sup>·A<sup>-</sup> geometries. Even using Møller-Plesset perturbation theory to second order (MP2) causes the double-minimum potentials for the AHA<sup>-</sup> ions to coalesce into a single flat-bottomed minimum.<sup>50</sup> High-resolution spectroscopy studies indicate these anions do, in fact, have centrosymmetric equilibrium structures.<sup>51</sup>

For an asymmetric ion such as CH<sub>3</sub>OHF<sup>-</sup>, we might expect to find a local minimum, CH<sub>3</sub>O<sup>-</sup>·HF, as well as the global one described by Figure 4 and Table III. Figure 5 shows a plot of the potential energy as a function of the position of the hydrogen atom between the O and F atoms which are assumed, along with all other degrees of freedom, to be fixed. The plot shows that at the Hartree-Fock level there is evidence of a plateau in the potential corresponding to the CH<sub>3</sub>O<sup>-</sup>·HF structure but that it disappears at the MP2 level. The MP2 correction clearly stabilizes geometries with the hydrogen more evenly shared between F and O; the potential shape is distinctly different. This has a large effect on the vibrational level spacings for the "O-H stretch" and the shape of the ground vibrational wave function along this coordinate. This will, in turn, have a profound effect on the intensity

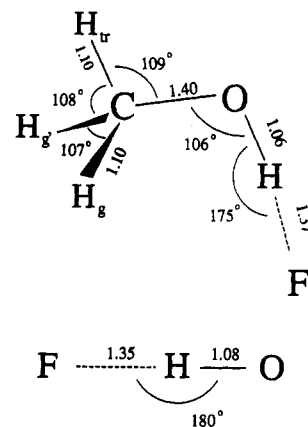


Figure 4. Calculated geometry for CH<sub>3</sub>OHF<sup>-</sup> (top) and OHF<sup>-</sup> (bottom). Bond lengths (Å) and angles (deg) are those calculated by full geometry optimization at MP2/6-31++G\*\*.

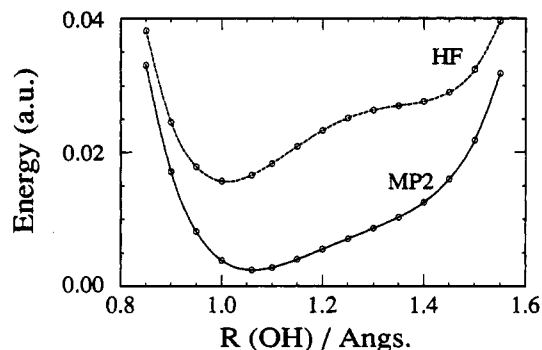


Figure 5. Potential energy profile along the hydroxyl hydrogen stretching coordinate in CH<sub>3</sub>OHF<sup>-</sup>. Cuts are calculated by fixing geometry parameters at the MP2/6-31++G\*\* equilibrium values and varying  $R_{\text{OH}}$ . To simplify calculations, the F-H-O angle is treated as linear (this increases the electronic energy by  $2 \times 10^{-4}$  au) and the  $R_{\text{OF}}$  is fixed at the sum of MP2 equilibrium  $R_{\text{OH}}$  and  $R_{\text{HF}}$ . CH<sub>3</sub>OHF<sup>-</sup> potential variation shown at the HF/6-31++G\*\* level (dashed, for absolute HF energy subtract 214.527 au) and at MP2/6-31++G\*\* (solid, for absolute MP2 energy subtract 215.077 au).

(47) Sheldon, J.; Bowie, J. *Aust. J. Chem.* **1983**, *36*, 289. Emsley, J.; Parker, R. J.; Overhill, R. E. *J. Chem. Soc., Faraday Trans. 2* **1983**, *79*, 1347.

(48) Botschwina, P.; Seibald, P.; Burmeister, R. *J. Chem. Phys.* **1988**, *88*, 5246.

(49) Sannigrahi, A. B.; Peyerimhoff, S. D. *J. Mol. Struct. (THEOCHEM)* **1988**, *165*, 55.

(50) Ikuta, S.; Saitoh, T.; Nomura, O. *J. Chem. Phys.* **1989**, *91*, 3539. Ikuta, S.; Saitoh, T.; Nomura, O. *J. Chem. Phys.* **1990**, *93*, 2530.

(51) Kawaguchi, K.; Hirota, E. *J. Chem. Phys.* **1987**, *87*, 6838. Kawaguchi, K. *J. Chem. Phys.* **1988**, *88*, 4186.

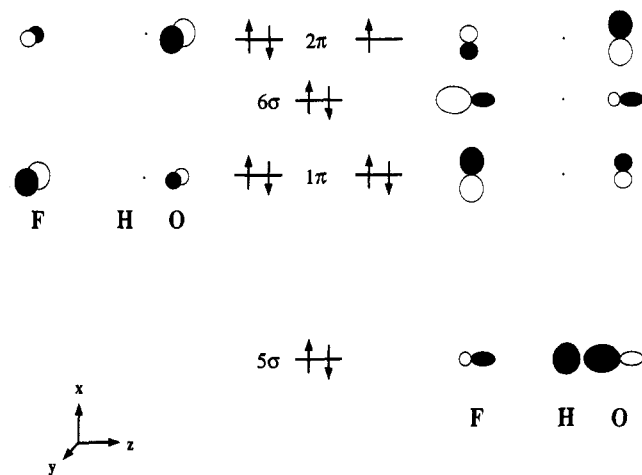


**Figure 6.** Schematic molecular orbital diagram for  $\text{OHF}^-$ . Orbital occupancy shown is for the  $^2\Pi$  ground state of anion.

distribution seen in the photoelectron spectrum.

The calculated harmonic vibrational frequencies for the  $\text{CH}_3\text{OHF}^-$  ion are shown in Table IV;  $\omega_3$  is the O–H stretching mode which corresponds to the potential function we have been discussing. The harmonic frequency for this mode ( $2215\text{ cm}^{-1}$ ) is strongly perturbed from its value in  $\text{CH}_3\text{OH}$  (MP2/6-31++G\*\* value  $3900\text{ cm}^{-1}$ ). The F–HOR stretching mode,  $\omega_9$ , is analogous to  $\omega_1$  in the bihalide ions and  $\text{OHF}^-$  (see below). These two stretching modes, the O–H stretch and the O–F stretch, are the two modes most important to understanding the photoelectron spectra.

The ab initio results for the ground  $^2\Pi$  state of the  $\text{OHF}^-$  anion are shown in Table VI and Figure 4. It is clear from the similarity in the equilibrium geometry of this ion and the OHF moiety in  $\text{CH}_3\text{OHF}^-$  that the  $\text{CH}_3$  group has little effect on the hydrogen bond, except to slightly bend it. It is worth noting that, in contrast to  $\text{CH}_3\text{OHF}^-$ ,  $\text{OHF}^-$  is open shelled but the spin remains localized on the oxygen atom, as in OH. The spin–orbit splitting in this state is expected to be smaller than the  $139\text{ cm}^{-1}$  of  $\text{OH}(^2\Pi)$ .<sup>37</sup> The expectation values of the spin operator,  $\langle S^2 \rangle$ , listed in Table VI indicate that spin contamination is not a problem in the unrestricted wave function; a pure doublet state has  $\langle S^2 \rangle = 0.75$ .

A schematic of the molecular orbitals for  $\text{OHF}^-$  is shown in Figure 6. This qualitative figure will be used later to explain the different neutral electronic states and their relationship to anion photodetachment. The  $^2\Pi$  ground electronic state is the configuration shown in Figure 6. There is a low-lying  $^2\Sigma^+$  state, which results on promoting a  $6\sigma$  electron to the  $2\pi$  orbital. This state has a single minimum at  $\text{O}^- \cdot \text{HF}$ ; it does not correlate to ground-state  $\text{OH} + \text{F}^-$ . Collinear potential cuts along the  $R_{\text{OH}}$  coordinate for the  $^2\Pi$  and  $^2\Sigma^+$  states are shown in Figure 7. The  $^2\Pi$  curve is very similar to that shown for  $\text{CH}_3\text{OHF}^-$  in Figure 5. Table VI contains the harmonic frequencies of the ground  $^2\Pi$  state. The O–H stretching frequency,  $2015\text{ cm}^{-1}$ , is significantly reduced from the value in free OH and is also lower than the same mode (also  $\omega_3$ ) of  $\text{CH}_3\text{OHF}^-$ . The O–F stretching frequency,  $\omega_1$ , at  $433\text{ cm}^{-1}$  is higher than  $\omega_9$  of  $\text{CH}_3\text{OHF}^-$ . These two frequencies will be used to describe the anion wave function in the simulation below. The bending vibration has two components for the linear ground state of  $\text{OHF}^-$ , as expected for a linear molecule in a degenerate electronic state.<sup>52</sup>

**Dissociation Energies.** Accurate ab initio estimates of bond dissociation energies are normally difficult to calculate. However, for dissociations that do not involve breaking of a bonding pair of electrons, as is the case here, correlation corrections are relatively small and ab initio methods can yield reliable energies.<sup>53</sup> As can

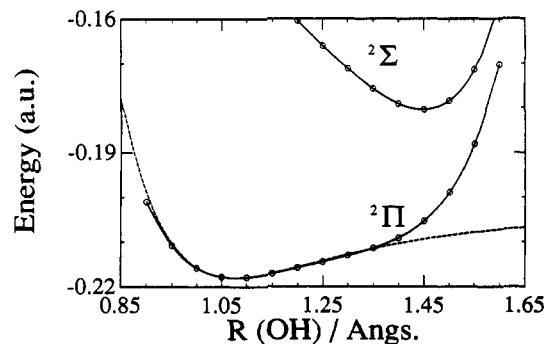


**Figure 7.** Potential energy profile for  $^2\Pi$  and  $^2\Sigma$  electronic states of  $\text{OHF}^-$  along hydrogen stretching coordinate at MP2/6-31++G\*\* (solid lines). Cuts calculated with  $R_{\text{OF}}$  held at the  $^2\Pi$  state equilibrium value. For absolute energies subtract 175 au. Dotted line shows Morse function used to approximate  $\text{OHF}^-$  hydrogen stretching potential for construction of anion wave packet.

be seen in Table V, even the Hartree–Fock estimate for the hydrogen bond strength of  $\text{CH}_3\text{OHF}^-$ , with respect to dissociation to  $\text{CH}_3\text{OH} + \text{F}^-$ , is in fairly close agreement with the experimental value ( $D_{\text{H}298} = 1.28\text{ eV}$ ). Handy et al.<sup>54</sup> have shown that the Møller–Plesset perturbation theory treatment is convergent and reliable for interaction energies if bond breaking or curve crossing does not occur. Chalasiński<sup>55</sup> demonstrated that MP2 calculations with standard basis sets, when corrected for basis set superposition error (BSSE), yield quantitative estimates of hydrogen bonding energies. It is important to recognize that for estimating correlation corrections to the hydrogen bond dissociation energies, the size-consistent MP methods are to be preferred over configuration interaction (CI) methods.

The calculated hydrogen bond dissociation energies  $D_0^0$  defined earlier, are shown in Tables V and VII.  $\text{OHF}^-$  is calculated to be more stable with respect to dissociation than  $\text{CH}_3\text{OHF}^-$ . As mentioned earlier, the binding strength of  $\text{CH}_3\text{OHF}^-$  has been measured<sup>25</sup> whereas that of  $\text{OHF}^-$  has not. To compare the ab initio value for  $\text{CH}_3\text{OHF}^-$  with the experimental value, we must convert  $D_0^0$  to a bond enthalpy at 298 K.<sup>55</sup> Using the MP2 harmonic frequencies of  $\text{CH}_3\text{OHF}^-$  (Table IV) and  $\text{CH}_3\text{OH}$ , and assuming that the change in the average rotational energy on dissociation is zero, we calculate  $\Delta H_{298}^0(\text{CH}_3\text{OHF}^- \rightarrow \text{F}^- + \text{CH}_3\text{OH}) = 1.32\text{ eV}$  (30.4 kcal/mol) at MP2 and 1.29 eV (29.8 kcal/mol) at MP4 compared to the experimental value of  $1.28 \pm 0.04\text{ eV}$  (29.6  $\pm$  1 kcal/mol).<sup>25</sup> It appears that the ab initio estimate is in very good accord with the experimental data, placing confidence in the MP4  $D_0^0$  estimate, 1.48 eV (34.0 kcal/mol), for  $\text{OHF}^-$ .

It should be noted that no correction is made for basis set superposition error in these calculations. Further, it appears that the correlation correction to fourth order for the  $D_0^0$  of  $\text{CH}_3\text{OHF}^-$  is more fully converged than that for  $\text{OHF}^-$ . Thus, it is probable that higher order corrections will be required for the latter ion. The fact remains that the  $\text{OHF}^-$  anion is predicted to have a stronger hydrogen bond than  $\text{CH}_3\text{OHF}^-$  at every level of correlation treatment. This is shown not only in the dissociation energy but also in the stronger perturbation to the O–H stretching frequency, the higher F–O stretching frequency, and the more central positioning of the hydrogen between the end atoms. This result is also supported by the experimental observation that the photoelectron band origin for  $\text{OHF}^-$  is shifted to lower electron kinetic energy by 0.3 eV over  $\text{CH}_3\text{OHF}^-$ .

**3. Simulation of the  $\text{OHF}^-$  Photoelectron Spectrum.** In this section, we simulate the  $\text{OHF}^-$  photoelectron spectrum using our ab initio results for  $\text{OHF}^-$  along with the ab initio potential energy surfaces developed for the  $\text{F} + \text{OH}$  reaction by Sloan and co-

(52) Herzberg, G. *Molecular Spectra and Molecular Structure III. Electronic Spectra of Polyatomic Molecules*; Van Nostrand Reinhold: New York, 1966; p 27.

(53) Hehre, W.; Radom, L.; Schleyer, P. v. R.; Pople, J. A. *Ab initio Molecular Orbital Theory*; John Wiley: New York, 1986; p 270.

(54) Handy, N. C.; Knowles, P. J.; Somasundram, K. *Theor. Chim. Acta* **1985**, *68*, 87. Knowles, P. J.; Somasundram, K.; Handy, N. C. *Chem. Phys. Lett.* **1986**, *113*, 8.

(55) Chalasiński, G.; Kendall, R. A.; Simons, J. *J. Chem. Phys.* **1987**, *87*, 2965.

workers.<sup>23</sup> By comparing the simulated and experimental spectra, we can learn about deficiencies in the F + OH potential energy surface. We have previously described a fully quantum dynamical method that will simulate the dissociative photoelectron spectrum of a linear triatomic AHB<sup>-</sup>.<sup>7</sup> This method, which is based on the wave packet propagation technique of Kosloff and Kosloff,<sup>56</sup> treats dynamics along the two stretching coordinates exactly. It assumes all nuclear motion takes place on a collinear potential energy surface.

An initial wave packet  $\phi(0)$ , which, within the Franck-Condon approximation, is the anion ground vibrational wave function, is propagated on the neutral potential energy surface according to

$$|\phi(t)\rangle = e^{-i\hat{H}t/\hbar}|\phi(0)\rangle \quad (7)$$

Here  $e^{-i\hat{H}t/\hbar}$  is the time evolution operator and  $\hat{H}$  is the Hamiltonian for the neutral surface. The overlap of  $\phi(t)$  with  $\phi(0)$  defines the time autocorrelation function  $C(t)$

$$C(t) = \langle \phi(0)|\phi(t)\rangle \quad (8)$$

and the Fourier transform of this complex function yields the photoelectron spectrum:<sup>57,58</sup>

$$\sigma(E) \propto \int_{-\infty}^{\infty} \exp(iEt/\hbar)C(t) dt \quad (9)$$

The simulation makes use of the collinear ab initio surfaces that have been developed for the lowest triplet and singlet channels of the F + OH system.<sup>23</sup> Sloan and co-workers evaluated energy points across the two surfaces using a multireference configuration interaction (MRCI) scheme, employing the multireference analogue of Davidson's correction<sup>59</sup> to extrapolate energies to full configuration interaction (FCI). To calculate the entire collinear surfaces, the authors were constrained to use of the relatively small 4-31G basis set. The surfaces were each fitted to a rotated Morse oscillator spline (RMOS) function.<sup>60</sup> The authors went on to show that the barrier height on the lowest triplet surface remained virtually unchanged when the basis set was improved to double- $\zeta$  plus polarization (DZP) quality. We shall first consider only the lowest surface for the collinear reaction  $F(^2P) + OH(^2\Pi) \rightarrow HF(^1\Sigma^+) + O(^3P)$  for our simulation. This surface has  $^3\Pi$  electronic symmetry, and a classical barrier of 12 kcal/mol at  $R_{OH} = 1.08 \text{ \AA}$  and  $R_{HF} = 1.32 \text{ \AA}$ .

Together with the neutral potential surface, we also require the wave function for the ground vibrational state of the anion. The wave function is assumed to be separable along the two normal coordinates,  $Q_1$  and  $Q_3$ . To construct this vibrational wave function, we use our MP2 values for the anion equilibrium geometry ( $R_{HF}^c$  and  $R_{OH}^c$ ) and frequencies ( $\omega_1$  and  $\omega_3$ ) for the two stretching vibrations. The following transformation from internal coordinates (in  $\text{\AA}$ ) to normal coordinates (in  $\text{amu}^{1/2}\text{\AA}$ ) is derived from the ab initio Cartesian force constant matrix:

$$Q_1 = 2.989(R_{HF} - R_{HF}^c) + 2.747(R_{OH} - R_{OH}^c) \quad (10)$$

$$Q_3 = 0.198(R_{HF} - R_{HF}^c) + 1.158(R_{OH} - R_{OH}^c) \quad (11)$$

Note that  $Q_1 \approx 3(R_{OF} - R_{OF}^c)$  and  $Q_3 \approx (R_{OH} - R_{OH}^c)$ .

In the simulations carried out for the  $\text{BrHI}^-$  photoelectron spectrum,<sup>7</sup> the experimental intensity distribution was impossible to model without including anharmonicity along the  $Q_3$  coordinate for the anion. The anion potential surface was therefore described by the sum of a Morse potential for the  $\nu_3$  mode and a harmonic potential for the heavy atom  $\nu_1$  stretching mode. For  $\text{OHF}^-$ , the MP2 potential energy cut along the  $R_{OH}$  coordinate can be fit to a Morse function; this is shown in Figure 7. The  $R_{OH}$  coordinate is an extremely good approximation to  $Q_3$  if  $R_{OF}$  is kept fixed, as seen in eqs 10 and 11, so the Morse potential in Figure 7 is

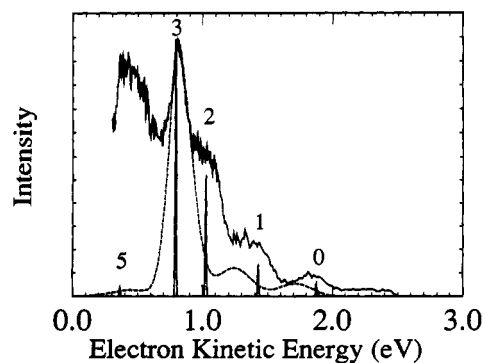


Figure 8. Simulated  $\text{OHF}^-$  photoelectron spectrum from two-dimensional wave packet propagation on the  $^3\Pi$  RMOS surface (dashed) superimposed on experimental spectrum (solid). Also shown is the result of a one-dimensional simulation (sticks) described in text. Labels above sticks refer to  $\nu_3$  quantum numbers (see Figure 11). Both simulations have been shifted by 0.22 eV to higher electron kinetic energy (see text).

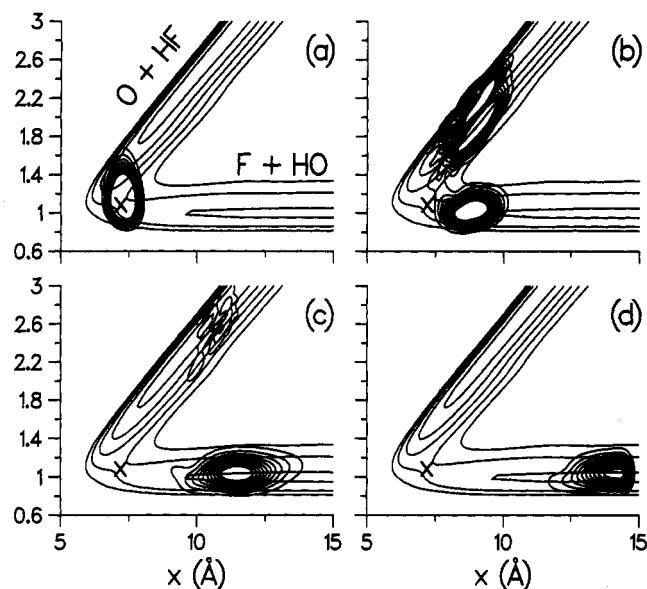


Figure 9. Wave packet dynamics on the RMOS  $^3\Pi$  potential surface. Equally spaced contours of  $|\psi(t)|$  are superimposed on contours of the potential energy for (a)  $t = 0$ , (b)  $t = 31$ , (c)  $t = 62$ , and (d)  $t = 93$  fs. The potential contours drawn are for energies 0.25, 0.75, 1.25, 1.75, and 2.25 eV above the bottom of the  $\text{O}(^3P) + \text{HF}$  well, and the saddle point is marked by an  $\times$ . The propagation is carried out in mass-scaled coordinates (defined in ref 7), which are also the coordinates used in the plots, on a grid with  $128 \times 64$  points along  $x$  and  $y$ , respectively. A 10-point absorbing strip boundary is used to absorb flux leaving grid (see ref 61). The initial wave packet (see text for details) is propagated for 7680 time steps of 1 au each.

assumed to be the potential energy along the  $Q_3$  coordinate. The one-dimensional fit to this function yields  $\omega_e = 2015 \text{ cm}^{-1}$  (as expected from Table VI) and  $\omega_e x_e = 350 \text{ cm}^{-1}$ . A harmonic potential is constructed along  $Q_1$  by using the MP2 frequency ( $433 \text{ cm}^{-1}$ ) from Table VI. The required initial wave packet,  $\phi(0)$ , is then set equal to the ground vibrational wave function of this anion potential surface.

The simulation is performed by propagating the initial wave packet on a grid in two dimensions, under the influence of the neutral collinear potential surface. The propagation is continued until all flux has left the grid. Absorbing boundaries are imposed at the edges of the grid;<sup>61</sup> this device greatly reduces the configuration space the grid must span and, thus, the calculation time. All computational details of the method are contained in ref 7, and the relevant parameters are listed in the figure captions for each simulation. Figure 8 shows the simulated photoelectron spectrum of  $\text{OHF}^-$  resulting from wave packet propagation on

(56) Kosloff, D.; Kosloff, R. *J. Comput. Phys.* **1983**, *52*, 35. Kosloff, R. *J. Phys. Chem.* **1988**, *92*, 2087.

(57) Heller, E. J. *Acc. Chem. Res.* **1981**, *14*, 368.

(58) Lorquet, A. J.; Lorquet, J. C.; Delwiche, J.; Hubin-Franskin, J. *J. Chem. Phys.* **1982**, *76*, 4692. Pollard, J. E.; Trevor, D. J.; Reutt, J. E.; Lee, Y. T.; Shirley, D. A. *J. Chem. Phys.* **1984**, *81*, 5302.

(59) Davidson, E. R. In *The World of Quantum Chemistry*; Daudel, R., Pullman, D., Eds.; Reidel: Dordrecht, Holland, 1974; p 17.

(60) Schatz, G. C. *Rev. Mod. Phys.* **1989**, *61*, 669.

(61) Bisseling, R. H.; Kosloff, R.; Manz, J. *J. Chem. Phys.* **1985**, *83*, 993.

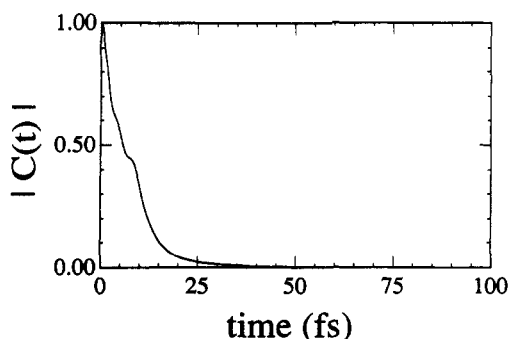


**Figure 10.** Absolute value of the time autocorrelation function calculated in the two-dimensional propagation on the  $^3\Pi$  RMOS surface.

the  $^3\Pi$  ab initio surface. The result is exact within the collinear approximation.

Figure 9 shows the wave packet dynamics that give rise to this simulation. The potential surface is plotted in the mass-scaled coordinates defined in ref 7; essentially  $x \approx 3R_{OF}$  and  $y = R_{OH}$ . These coordinates almost exactly parallel the normal coordinates of the ion  $Q_1$  and  $Q_3$ . The first frame (Figure 9a) shows the initial wave packet, corresponding to the anion wave function. The asymmetric shape of the wave packet derives from the pronounced anharmonicity along  $Q_3$ . The wave packet sits right over the saddle point of the reaction surface (marked in the Figure with a cross), underlining the sensitivity of the photoelectron spectrum to features of the surface at the saddle point and to the magnitude of the barrier height. The initial wave packet also extends into both the reactant valley and around the reaction "corner" into the product valley.

The following frames of Figure 9 show the bifurcation of the wave packet into both valleys; the subsequent disappearance of the wave packet out to fragments is very swift. The component of the wave packet exiting out to  $O(^3P) + HF$  has a faster rate of disappearance from the Franck-Condon region than the component traveling down to the entrance valley. The latter component, moving parallel to the  $x$  axis and out to  $F + OH$ , shows little vibrational excitation as compared to that moving in the  $O(^3P) + HF$  exit valley, where considerable nodal structure, corresponding to HF vibrational excitation, is seen perpendicular to the direction of motion. In Figure 9d the last component of the wave packet is seen leaving the grid; the shape of the wave packet is distorted here because of the absorbing boundary.

In accord with the extremely fast movement of the wave packet away from its nascent position on the neutral potential energy surface, the autocorrelation function shows very fast decay and evidence of only a weak recurrence. The absolute value of the autocorrelation function,  $|C(t)|$ , is plotted in Figure 10. The fast fall time is in strong contrast with the long-lived recurrences in the autocorrelation functions calculated for bihalide photodetachment.<sup>7,62,63</sup> The Fourier transform of this autocorrelation function yields a broad, but structured, simulated photoelectron spectrum, and it is this that is shown with the dashed line in Figure 8.

In this simulation, the two low-intensity peaks between the product and reactant asymptotes are from transitions to states of the complex that correlate to different product HF vibrational levels. The single, more intense feature near the reactant asymptote is narrower than the other peaks (fwhm  $< 200$  meV versus  $\approx 300$  meV). This peak is most likely due to the component of the wave packet moving out along the entrance valley to  $F + OH$ , which, as noted above, leaves the Franck-Condon region more slowly than that departing along the exit valley.

To confirm these "assignments", we have performed a one-dimensional simulation that treats only the potential along the  $y$ , or  $R_{OH}$ , coordinate with the mass-weighted coordinate  $x$  fixed

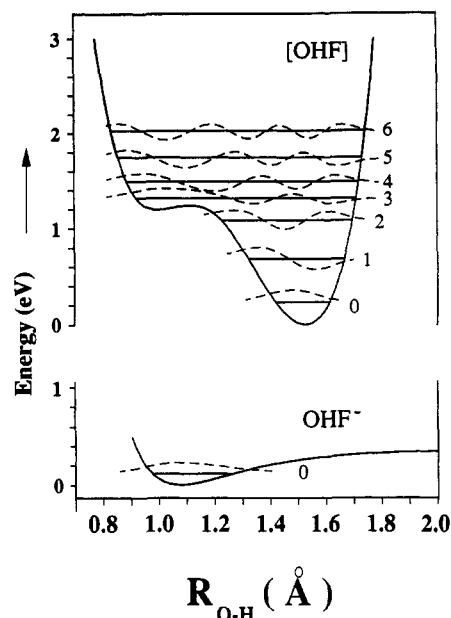


**Figure 11.** One-dimensional potentials for the  $\nu_3$  mode in  $OHF^-$  and  $[OHF]$ . Anion potential (bottom) is the Morse potential shown in Figure 7; neutral effective potential (upper) is a cut through the  $^3\Pi$  RMOS surface at constant  $x = x_e$  (see text). Calculated eigenstates are labeled by their  $\nu_3$  quantum numbers.

at its value for the ion equilibrium geometry,  $x_e$ . This, to a good approximation, is the effective potential for the hydrogen stretching  $\nu_3$  mode.<sup>7</sup> In Figure 11 these one-dimensional potentials for the anion and neutral are shown along with the first few eigenvalues and eigenfunctions supported by each potential. The anion potential is the  $^2\Pi$  Morse potential shown in Figure 7, and the neutral potential results from taking a cut through the fitted ab initio  $F + OH$  surface at  $x = x_e$ . By computing the Franck-Condon overlap between the ground-state wave function supported by the anion potential with the first few neutral wave functions, a simulated stick spectrum, shown also in Figure 8, is generated.

The one-dimensional stick spectrum consists of a progression in the  $\nu_3$  mode of the  $[OHF]$  complex; the peak labels in Figure 8 correspond to the energy levels in Figure 11. Peaks 0, 1, and 2 result from transitions to the  $O + HF$  product (exit) valley, while an inspection of the one-dimensional neutral wave functions (Figure 11) shows that the  $\nu_3 = 3$  level is localized in the  $F + OH$  reactant (entrance) valley. Peak 3 in the one-dimensional simulation lines up with the intense peak in the two-dimensional simulation, indicating that the latter is indeed due to a state of the complex localized in the reactant valley. Peaks 0 and 1 apparently correspond to the two peaks in the two-dimensional simulation between the reactant and product asymptotes, although the one-dimensional peaks occur at slightly higher electron kinetic energy. The comparison between the simulations suggests that peak 2 is hidden as a shoulder in the two-dimensional simulation. In fact, the intense peak in the two-dimensional simulation has a definite asymmetry, and it can be readily confirmed that there is an intensity contribution, corresponding to the  $\nu_3 = 2$  stick, on the high electron energy side of this peak. The one-dimensional treatment is approximate in that it does not consider overlap at different values of  $x$ , and the time scale separation of  $x$  and  $y$  is strictly only appropriate for extreme heavy-light-heavy systems.<sup>5</sup> It is these inadequacies that are presumably responsible for the one-dimensional sticks not coinciding with the centers of the two-dimensional peaks. However, this analysis does provide some insight into the appearance of the two-dimensional simulation.

Let us now compare the simulated and experimental spectra (Figure 8). The two-dimensional peak widths and the spacings of the product progression agree reasonably well with experiment, and the intensity distribution is in qualitative agreement with the experimental profile. The overall agreement between experimental and simulated peak widths is particularly striking as it indicates

(62) Metz, R. B.; Bradforth, S. E.; Neumark, D. M. *Adv. Chem. Phys.*, in press.

(63) Engel, V. *J. Chem. Phys.* 1991, 94, 16.

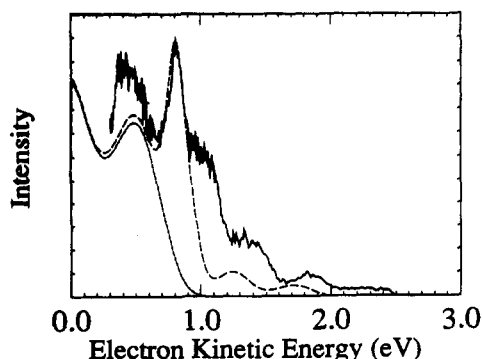


**Figure 12.** Simulated  $\text{OHF}^-$  photoelectron spectrum showing contribution of  $^3\Pi$  and  $^1\Delta$  electronic surfaces. Component deriving from the  $^1\Delta$  surface is shown by a short dashed line. The sum of two states' simulated photoelectron profiles, convoluted with the experimental resolution function, is shown by a dashed line. Each state's profile simulated via independent wave packet propagations; both have been shifted to higher electron kinetic energy by 0.22 eV (see text). The initial wave packet and propagation parameters are identical in two simulations, and are those given in the caption of Figure 9.

that rapid dissociation on a collinear surface can explain the broad experimental peaks. On energetic grounds we assign peaks A–D to states of the  $[\text{OHF}]$  complex that dissociate to  $\text{O} + \text{HF}$  products. On the basis of one- and two-dimensional simulations, we assign the intense experimental peak at 0.80 eV (E, Figure 3) as a *reactant* peak: a state of the  $[\text{OHF}]$  complex that dissociates to  $\text{F} + \text{OH}$  reactants.

However, in Figure 8, the one- and two-dimensional simulations have been shifted by 0.22 eV to higher electron kinetic energy so that the experimental peak E lines up with the most intense simulated peak. An even larger shift would be expected if the simulation had been performed on a comparable three-dimensional potential energy surface rather than the collinear surface used here; this additional shift will be approximately equal to the bending zero-point energy near the saddle point on the three-dimensional surface.<sup>64,65</sup> This bending zero-point energy is estimated to be  $\approx 0.05$  eV.<sup>66</sup> Thus, simulations on a comparable three-dimensional surface would need to be shifted by about 0.27 eV to higher electron kinetic energy. The significance of this shift is discussed in the following section.

In our analysis of the bihalide spectra,<sup>5,7</sup> we commented extensively on the role of excited electronic states of the neutral in our photoelectron spectra, and contributions from excited states are likely in the spectra presented here as well. For the  $\text{F} + \text{OH}$  system, we can explicitly model the contribution of one excited state, the  $^1\Delta$  state, to the photoelectron spectrum, because a potential energy surface is available for this state.<sup>23</sup> We shall defer a full discussion of the electronic structure of this and other excited states until later, but here we show the results of performing an identical simulation, using the RMOS  $^1\Delta$  surface of Sloan and co-workers, to that described above for the  $^3\Pi$  surface. The wave packet dynamics should be quite different on the  $^1\Delta$  surface, which adiabatically connects  $\text{F} + \text{OH}(^2\Pi)$  to  $\text{HF}(^1\Sigma^+) + \text{O}(^1\text{D})$ . This is an endoergic process for which the barrier is expected to lie on the  $\text{O}(^1\text{D}) + \text{HF}$  side of the potential energy surface, and this is borne out by the ab initio calculated surface. Thus, photodetachment to the  $^1\Delta$  surface should result in less overlap with the saddle point region than photodetachment to the  $^3\Pi$  surface.

Figure 12 shows the contribution of the  $^1\Delta$  simulation to the overall photoelectron spectrum. Both the  $^3\Pi$  and  $^1\Delta$  simulations have been shifted to higher electron kinetic energy by the same 0.22 eV discussed above. The electronic transition dipole moments for transition from ion ground state to the neutral  $^3\Pi$  and  $^1\Delta$  states

have been set in the ratio 1:5 to best reproduce experiment, in the absence of any other data. By including the  $^1\Delta$  state, the simulation now reproduces the broad experimental peak (F) at 0.45 eV. The overall agreement between the simulated and experimental spectra is quite remarkable considering that all potential parameters are the "raw" ab initio ones, including the energy separation between the two electronic-state progressions. This would seem to be strong evidence for the overlapping contribution of excited states in the experimental photoelectron spectrum.

## Discussion

**1.  $\text{OHF}^-$  Photoelectron Spectrum.** Let us return to consider the neutral reaction surface that dominates the  $\text{OHF}^-$  photoelectron spectrum, the  $^3\Pi$  surface. We wish to assess how realistic this surface is and apply what we learn to the fluorine + alcohol reaction surfaces. Although there is qualitative agreement between the simulated and experimental profiles, there are some serious deficiencies. We shall discuss these discrepancies, and some possible causes, in the hope of obtaining a more detailed picture of the neutral potential energy surface in the transition-state region.

The three major areas in which the theoretical fit differs from the experimental spectrum are (i) the number of peaks in the product vibrational progression and their positions relative to the reactant peak, (ii) the large shift required for the entire simulation, and (iii) the intensity distribution of peaks corresponding to product states. These deviations are almost certainly due to discrepancies in the neutral potential energy surface and/or the equilibrium properties of the anion. Because ab initio descriptions of potential minima are known to be predicted to a higher degree of accuracy than points on a global surface far away from minima, we shall make the assumption in the following discussion that the anion structure and dissociation energy have been correctly described and that all changes need to be made to the neutral surface. This is not likely to be completely true but merely reflects the likely relative error bars on the two calculations.

One obvious problem is that the reaction exoergicity on the RMOS  $^3\Pi$  surface is incorrect. The RMOS fit to the FCI/4-31G exoergicity is 1.198 eV as compared to the experimental value, 1.502 eV. (These figures reflect bottom of the well energies for the diatomic molecules.) Sloan et al. have shown that this problem stems mainly from the basis set used in the ab initio calculation.<sup>23</sup> This gross defect is certainly contributing to the absence of any structure in the simulation at electron kinetic energies higher than 2.0 eV (Figure 8). With the surface as is, it is energetically impossible for a state to exist with an energy corresponding to the step at highest eKE in the experimental spectrum. Clearly, in any attempt to improve the simulation by changing the neutral potential energy surface, the exoergicity should be corrected.

The other feature of the  $\text{F} + \text{OH}^3\Pi$  surface that calls for some adjustment is the barrier height. A major discrepancy between the simulation on the RMOS surface and the experimental spectrum was that the simulated band origins had to be displaced to higher electron kinetic energy to get the largest feature (assigned to the reactant channel) to match the experimental peak. For the  $^3\Pi$  surface, the saddle point lies in the center of the Franck–Condon region, so lowering the barrier height will shift the spectrum in the required direction. As the shift required, 0.27 eV, is considerably larger than the expected error in the ion binding energy ( $< 0.15$  eV), it seems probable that the barrier on the reaction surface is indeed too high.

To show the effect of using a smaller barrier, we have performed two further simulations. We first scaled<sup>67</sup> the RMOS surface so as to reproduce the experimental exoergicity; this yielded a surface we shall call RMOS-A. A further round of scaling<sup>68</sup> was per-

(64) Bowman, J. M. *Adv. Chem. Phys.* **1985**, *61*, 115.

(65) Schatz, G. C.; Kuppermann, A. *Phys. Rev. Lett.* **1975**, *35*, 1266.

(66) This estimate is based on the bending frequency calculated at the saddle point of several three-dimensional LEPS model surfaces that describe the  $\text{F} + \text{HO}$  system and have similar barrier heights to the collinear surface used in the present simulation.

(67) The parameters defining the RMOS surface were changed such that  $D(\theta)$  (describing the energy along the minimum-energy path) was smoothly corrected with a function that varied as  $\sin(\theta)$ .  $\beta(\theta)$  was adjusted to maintain the original harmonic frequency along each Morse ray. The  $I_e(\theta)$  parameter was left unchanged. See ref 23 for the definition of the RMOS parameters.

(68) The  $D(\theta)$  values were smoothly corrected with a function that varied as  $\sin(2\theta)$ , and once again  $\beta(\theta)$  was corrected to maintain original harmonic frequency along each ray while  $I_e(\theta)$  was unchanged.

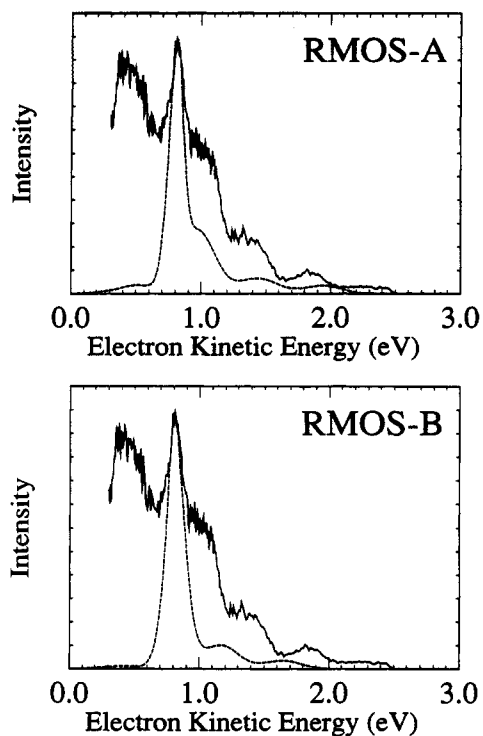


**Figure 13.** Simulated  ${}^3\Pi$  band (dashed) of  $\text{OHF}^-$  photoelectron spectrum using the two scaled RMOS surfaces (see text), superimposed on the experimental spectrum (solid). (a) The RMOS-A surface has the correct reaction exoergicity; the simulated spectrum has been shifted to higher electron kinetic energy by 0.23 eV. (b) The RMOS-B surface has the correct exoergicity and a reduced barrier height of 0.29 eV. This simulated spectrum has *not* been shifted. The initial wave packet and propagation parameters for both simulations are once again identical with those in Figure 9.

formed on RMOS-A in order to approximately halve the barrier to 0.24 eV (5.5 kcal/mol). This surface we denote RMOS-B. These surfaces are not suggested as optimized potential functions that reproduce our data, but they do demonstrate the result of some very simple improvements over the pure *ab initio* surface. The simulated photoelectron spectra calculated on each of these surfaces, while ignoring the  ${}^1\Delta$  state, are shown in Figure 13. The changes are significant. The RMOS-A simulation shows three, rather than two, resolved members of the product vibrational progression. In particular, a feature corresponding to experimental peak D now appears. However, the entire simulated spectrum must still be shifted, again to higher electron kinetic energy, to align the simulated reactant peak with the experimental peak E; for this surface the shift is 0.23 eV, or 0.28 eV including the zero point bend correction.

In the RMOS-B simulation (Figure 13b), when including the zero point bend correction, no shift is required to line up experimental peak E with the intense peak in the simulation. Decreasing the barrier height has thus removed the discrepancy between the energetics in the simulated and experimental spectra. The simulated peaks are still quite broad, in agreement with experiment. However, only two product peaks are discernible in the RMOS-B simulation, just as in the first simulation in Figure 8. As in that simulation, the third peak in the product progression is hidden under the intense reactant peak. Essentially, in comparison to the RMOS-A simulation, lowering the barrier has shifted the intense reactant peak to higher electron kinetic energy while not affecting the product peaks, thereby obscuring the third product peak that appeared in the RMOS-A simulation.

One important feature we have not attempted to change is the location of the saddle point on the  $\text{F} + \text{OH}$  surface. This is likely to have a major effect in a simulation. In particular, if the barrier occurred earlier in the  $\text{F} + \text{OH}$  reactant valley, the anion would have better overlap with states of the  $[\text{OHF}]$  complex that dissociate to  $\text{O} + \text{HF}$  products, and these states would be shifted

in energy closer toward the product asymptote.

In any case, the simulation on the RMOS-B surface has shown that a lower barrier can eliminate the need to shift the spectrum. Considering the errors in the calculated ion binding energy and the approximate treatment of the zero point bending energy, we conclude that a realistic barrier height for the  ${}^3\Pi$  surface is in the range 0.09–0.39 eV (2–9 kcal/mol). This result is significant as it implies that even at room temperatures direct hydrogen abstraction may compete with the nonadiabatic pathway suggested by Sloan et al.

Is this proposed barrier height reasonable? By comparison to other reactions of fluorine, the original *ab initio* barrier, 12 kcal/mol, might be considered unreasonably large for an abstraction reaction of this type. In general, *ab initio* reaction barriers reported are consistently too high, even with what must be considered current state-of-the-art methods.<sup>69,70</sup> It is very likely that problems of incomplete basis set, and thus errors resulting from basis set superposition error, will be manifested in the raw fitted *ab initio* surface used here.

The Evans–Polanyi relationship<sup>71</sup> between reaction exoergicity and barrier height states that the larger the exoergicity, the lower and earlier the classical barrier is on the reaction potential surface. This postulate has been well tested for hydrogen abstraction reactions. From this postulate, it would be expected that the reactions studied here would occur on surfaces with barriers comparable with that for  $\text{F} + \text{H}_2$  and smaller than that for  $\text{F} + \text{H}_2\text{O}$  (see exoergicities in Table I). Stevens et al.<sup>72</sup> have estimated a 4 kcal/mol barrier for  $\text{F} + \text{H}_2\text{O}$ ; the classical barrier height for  $\text{F} + \text{H}_2$ , although subject to some controversy, is currently considered to be 1.4–2.5 kcal/mol.<sup>69,70</sup> The larger exoergicity for  $\text{F} + \text{OH}$  and  $\text{F} + \text{HOR}$  would seem to indicate that the barriers for direct abstraction for both reactions should be in the range 1–2 kcal/mol. The result of our simulations, while in agreement with a substantially lower barrier than that calculated *ab initio* for  $\text{F} + \text{OH}$ , seem to suggest a barrier somewhat higher than that predicted by the Evans–Polanyi relationship.

It is to be hoped that an *ab initio* reaction potential surface of improved quality can be generated which will confirm the lower barrier height for the direct abstraction process. In order to fully model the spectrum, it may be necessary to develop excited-state potential energy surfaces as well. The role of low-lying excited surfaces is explored in section 3 below.

**2.  $\text{CH}_3\text{OHF}^-$  and  $\text{C}_2\text{H}_5\text{OHF}^-$  Photoelectron Spectra.** The above discussion and simulations on the  $\text{F} + \text{OH}$   ${}^3\Pi$  surface serve as a model for understanding the photoelectron spectra of the alcohol complexes. The similarity of the  $\text{OHF}^-$  spectrum to those of the polyatomic systems encourages one to think that the effect of the alkyl group is small and that the  $\text{ROHF}^-$  spectra can be largely explained by the analysis of the  $\text{OHF}^-$  spectrum. In particular, the basic step structure and the peak widths observed can be understood in terms of the two-dimensional model above, the differences in intensity distributions in the three spectra are explained by the differing position of the bridging hydrogen in the ion, and the missing low electron energy peak in the  $\text{ROHF}^-$  spectra (peak F in the  $\text{OHF}^-$  spectrum, Figure 3) is attributable to the differing electronic structure in the  $[\text{ROHF}]$  and  $[\text{OHF}]$  complexes (see below).

However, as pointed out above, the features in the  $\text{ROHF}^-$  spectra are, in general, broader than those in the  $\text{OHF}^-$  spectrum. One could blithely attribute this to the presence of additional vibrational modes in the polyatomic systems. We would like to examine this more quantitatively to ascertain which, if any, of these vibrational modes play a major role in the appearance of the  $\text{ROHF}^-$  photoelectron spectra. We do this by attempting to determine which of the additional modes in the polyatomic  $\text{ROH}$  and  $\text{RO}$  fragments are excited subsequent to  $\text{ROHF}^-$  photode-

(69) Schaefer, H. F. *J. Phys. Chem.* **1985**, *89*, 5336.

(70) Bauschlicher, C. W., Jr.; Walch, S. P.; Langhoff, S. R.; Taylor, P. R.; Jaffe, R. L. *J. Chem. Phys.* **1988**, *88*, 1743.

(71) Evans, M. G.; Polanyi, M. *Trans. Faraday Soc.* **1938**, *34*, 11.

(72) Stevens, P. S.; Brune, W. H.; Anderson, J. G. *J. Phys. Chem.* **1989**, *93*, 4068.

tachment. These are referred to as "bath" modes; in the case of  $\text{CH}_3\text{OH}^-$  photodetachment, these include all the  $\text{CH}_3\text{O}$  vibrations and all the  $\text{CH}_3\text{OH}$  vibrations except the O-H stretch.

We consider which fragment modes are excited solely on the basis of the differences between the geometry of the neutral complex created by photodetachment and the equilibrium geometries of the fragments. This is a variation of the "Franck-Condon picture" which has been shown to provide a reasonable zero-order description of fragment excitation in photodissociation experiments.<sup>73</sup> In the classical picture of photodetachment, the nuclear configuration of the neutral complex formed is the same as the equilibrium geometry of the ion. The displacement of the C, H, and O atoms in the  $[\text{CH}_3\text{OHF}]$  complex from the equilibrium geometry of free  $\text{CH}_3\text{OH}$  and  $\text{CH}_3\text{O}$  will then lead to vibrations in the bath modes of these species. Mapping these displacements into changes along each of the normal coordinates of the free fragment, we can estimate the degree of vibrational excitation in each of the fragment modes. As a guide, we shall use the ab initio changes in bond lengths and angles in the methoxy frame from  $\text{CH}_3\text{OH}^-$  to  $\text{CH}_3\text{OH}$  and  $\text{CH}_3\text{O}$ .

The ab initio calculations (Table III) show that the changes in geometry in the  $\text{CH}_3\text{O}$  frame between  $\text{CH}_3\text{OH}^-$  and  $\text{CH}_3\text{OH}$ , while small, are principally in the C-O bond length and the bond angles about the carbon atom; the  $\angle\text{COH}$  angle is not dramatically altered. Further, the calculated MP2 force field of  $\text{CH}_3\text{OH}$  gives us the normal coordinates for this molecule. By performing the transformation of the MP2 internal-coordinate changes into  $\text{CH}_3\text{OH}$  normal coordinates displacements, we determine which bath modes receive excitation in this simplified photodetachment process. The only mode appreciably excited is  $\nu_7$  ( $\text{CH}_3$  rock), whose observed fundamental frequency is  $1060\text{ cm}^{-1}$ .<sup>35</sup> The degree of vibrational excitation is, however, still small; if we compute Franck-Condon factors assuming two harmonic oscillators of the same frequency, for anion and neutral, displaced by the calculated value, a short progression is predicted with a  $(\nu = 1)/(\nu = 0)$  peak intensity ratio of 14%.

The changes in geometry from  $\text{CH}_3\text{OH}^-$  to  $\text{CH}_3\text{O}$  are also small; for the  $\text{CH}_3\text{O}$  equilibrium geometry we use the UMP2/6-31++G\*\* optimized structure calculated in  $C_s$  symmetry, which describes the lower Jahn-Teller component ( $A'$ ).<sup>42</sup> Performing the internal-coordinate transformation into displacements of  $\text{CH}_3\text{O}(2A')$  normal coordinates (this time derived from the UHF/6-31++G\*\* force field of  $\text{CH}_3\text{O}$ ), we determine that no mode is significantly excited; i.e., no mode has  $(\nu = 1)/(\nu = 0)$  intensity ratio greater than 5%.

This "Franck-Condon picture" therefore predicts relatively small effects in the  $\text{CH}_3\text{OH}^-$  spectrum from the presence of additional vibrational modes. While this treatment is quite approximate in that it is largely independent of the details of the potential energy surface in the  $\text{F} + \text{CH}_3\text{OH}$  transition-state region, we point out that the product-state-resolved studies<sup>19</sup> show that only 2% of the energy released in the  $\text{F} + \text{CH}_3\text{OH}$  reaction appears as vibrational excitation in the  $\nu_3$  C-O stretching mode of  $\text{CH}_3\text{O}$ . Although this was the only product vibrational mode investigated, these results suggest that the bath modes play only a minor role in the dynamics of the  $\text{F} + \text{CH}_3\text{OH}$  reaction.

We still are faced with the question of explaining the differences in widths in the  $\text{OH}^-$  and  $\text{CH}_3\text{OH}^-$  photoelectron spectra. Our ab initio calculations indicate that the COH angle remains strongly bent in  $\text{CH}_3\text{OH}^-$ , as in  $\text{CH}_3\text{OH}$ . Therefore, some of the energy released in the dissociation of the  $[\text{CH}_3\text{OHF}]$  complex to  $\text{HF} + \text{CH}_3\text{O}$  (by far the more exothermic channel) is likely to end up in rotational motion of both fragments. This rotational excitation may well provide a mechanism for adding width to the peaks that correspond to  $\text{HF} + \text{CH}_3\text{O}$  product states.

It is also worth noting that the precursor  $\text{OH}^-$  and  $\text{CH}_3\text{OH}^-$  anions are most likely characterized by a nonzero temperature, and some degree of vibrational excitation will be present. In  $\text{OH}^-$ , the O-F vibration is calculated to have the lowest frequency ( $\omega_1 = 433\text{ cm}^{-1}$ ), whereas in  $\text{CH}_3\text{OH}^-$  there are three low-fre-

TABLE VIII: Possible Low-Lying Electronic States of  $[\text{OHF}]$  Accessed in the Photoelectron Spectrum of  $\text{OH}^-$

	PUMP4- (SDTQ-FC) <sup>a</sup> /6-31G** energy at anion equilibrium geometry <sup>b</sup>		electronic configuration (with reference to Figure 6)
	au	eV	
$^3\Pi$	-175.033 816	0.0	...5 $\sigma^2$ 1 $\pi^4$ 2 $\pi_x^1$ 2 $\pi_y^2$ 6 $\sigma^1$
$^3\Sigma^-$	-175.009 523	0.6	...5 $\sigma^2$ 1 $\pi^4$ 2 $\pi_x^1$ 2 $\pi_y^1$ 6 $\sigma^2$
$^1\Pi$	-174.931 654	2.8	...5 $\sigma^2$ 1 $\pi^4$ 2 $\pi_x^1$ 2 $\pi_y^2$ 6 $\sigma^1$
$^1\Delta$	-174.911 790	3.3	...5 $\sigma^2$ 1 $\pi^4$ 2 $\pi_y^2$ 6 $\sigma^2$

<sup>a</sup>Spin projected UMP4 energies (see ref 76). <sup>b</sup>MP2/6-31++G\*\* anion geometry used; see Table VI.

quency modes (Table IV):  $\omega_9 = 391\text{ cm}^{-1}$  (O-F stretch),  $\omega_{10} = 167\text{ cm}^{-1}$  (FOC bend), and  $\omega_{15} = 77\text{ cm}^{-1}$  (hindered rotation). Assuming the two anions are formed at the same temperature, the excitation of the additional low-frequency modes in  $\text{CH}_3\text{OH}^-$  could lead to broader features in the photoelectron spectrum.

**3. Electronic Effects.** In the analysis of the photoelectron spectra of  $\text{BrHI}^-$ ,  $\text{ClHI}^-$ , and  $\text{FHI}^-$ , we presented<sup>7</sup> a full discussion of the role of multiple neutral electronic surfaces. For the  $\text{F} + \text{CH}_3\text{OH}$  and  $\text{F} + \text{C}_2\text{H}_5\text{OH}$  systems the situation is similar to those  $\text{X} + \text{HY}$  systems. In the entrance valley, the 3-fold spatial degeneracy of the  $^2\text{P}$  F atom (neglecting spin-orbit interactions) is broken by the approach of ROH, and all three resultant states may contribute to the photoelectron spectra. The states that correspond to approach of F on the H-O axis of HOR with the unpaired electron in a  $\pi$  type orbital will be much more repulsive than the ground-state  $\sigma$  type interaction. Morokuma and Yamashita<sup>74</sup> have shown from ab initio work that there is a contribution from the first electronically excited neutral state in the photoelectron spectrum of  $\text{ClHCl}^-$  that closely overlaps the band to the ground state. Experimentally, we have recently determined that transitions to excited  $\text{F} + \text{H}_2$  potential energy surfaces overlap transitions to the ground-state surface in the photoelectron spectrum of  $\text{FH}_2^-$ .<sup>75</sup> It is reasonable to expect this to occur in the  $\text{ROHF}^-$  spectra also.

For  $\text{F} + \text{OH}$  there are many more low-lying electronic states than for  $\text{X} + \text{HY}$ , even when ignoring spin-orbit coupling and constraining the geometry to be linear. These can be considered either by constructing a full correlation diagram or by using the molecular orbitals of the anion (Figure 6) and depicting the various  $[\text{OHF}]$  states formed upon removal of an electron. The latter is simpler and more useful as it includes the selection rule for a photodetachment process, namely, that only one-electron processes are allowed. This reduces the number of neutral states to be considered. Sloan et al. considered four potential surfaces,  $^3\Pi$ ,  $^3\Sigma^-$ ,  $^1\Delta$ , and  $^1\Pi$ , all of which are accessible from the  $^2\Pi$  anion.<sup>23</sup> We have already looked at two of these potential energy surfaces in the simulation section.

To estimate whether the other states will play a role in the photoelectron spectrum we have performed an ab initio calculation for the electronic energy of each state at the anion geometry. Table VIII shows these energies and the electronic configurations of each state with reference to anion molecular orbitals shown in Figure 6. These energies, which should be viewed as crude estimates only, indicate roughly where maximum intensity will occur in a photoelectron band to this state. They do not indicate where the onset of vibrational (or continuum) structure assignable to the respective surface would occur in the photoelectron spectrum. The energies in Table VIII are calculated by using single-reference wave functions that also suffer from spin contamination; the effects of the latter have been projected out by the standard method available in the GAUSSIAN 88 program.<sup>76</sup> The above ab initio problems were not an issue for the anion calcu-

(74) Yamashita, K.; Morokuma, K. *J. Chem. Phys.* **1990**, *93*, 3716.

(75) Weaver, A.; Metz, R. B.; Bradforth, S. E.; Neumark, D. M. *J. Chem. Phys.* **1990**, *93*, 5352. Weaver, A.; Neumark, D. M. *Discuss. Faraday Soc.*, in press.

(76) Schlegel, H. B. *J. Chem. Phys.* **1986**, *84*, 4530.

(73) Band, Y. B.; Freed, K. F. *J. Chem. Phys.* **1975**, *63*, 3382.

lations presented earlier. In comparison to the results in Table VIII, the multireference calculation of Sloan et al.<sup>23</sup> orders the states slightly differently:  $^3\Pi$ ,  $^3\Sigma$ ,  $^1\Delta$ ,  $^1\Pi$ . Further the RMOS fitted surface yields a  $^3\Pi$ - $^1\Delta$  separation at the anion geometry of only 0.63 eV. Apparently, all four surfaces should be considered before assigning all of the experimental spectrum's features. In addition, the inclusion of the spin-orbit interaction will result in even more potential energy surfaces to be considered.

### Summary

We have shown that the photoelectron experiment successfully probes the transition state of an asymmetric triatomic hydrogen abstraction reaction, namely, the F + OH reaction. The nature of the system, where all atoms are first row and consequently few electrons are involved, makes it amenable to a high-level ab initio potential surface characterization. We hope the results presented here will stimulate such theoretical interest. The photoelectron spectra of  $\text{CH}_3\text{OH}^-$  and  $\text{C}_2\text{H}_5\text{OH}^-$  have demonstrated the extension of our method to polyatomic reactions and have shown that vibrational structure at the transition state can still be resolved even when the transition species has 10 atoms. The interpretation of our spectra is relatively simple at a qualitative level and mirrors the work on the bihalide systems. A simulation that explicitly treats the collinear dynamics of F + OH, using a multireference ab initio potential surface, has been performed and yields reasonable agreement with the experimental result.

However, a detailed understanding of the spectra is clouded by a number of difficult theoretical questions. The simulation for the F + OH system assumes that the transition state is collinear and ignores the effect of the bending degree of freedom on the dissociation dynamics and, thus, on the photoelectron spectra. Schatz<sup>77</sup> has reviewed the theoretical formalism of photodetachment to the transition state of a bimolecular reaction in three dimensions. Schatz has also compared the results of exact collinear treatments, like this one, with three-dimensional  $J = 0$  coupled

channel hyperspherical (CCH) simulations for the  $\text{ClHCl}^-$  and  $\text{IHI}^-$  photoelectron spectra. He finds good agreement in the qualitative features. For the bihalide systems, the assumption of a collinear transition state is more reasonable than it is here. There is considerable evidence<sup>78</sup> that the  $\text{O}(^3P) + \text{HCl} \rightarrow \text{OH} + \text{Cl}$  reaction proceeds via a bent transition state; Gordon et al.<sup>79</sup> have calculated the saddle point geometry and find  $\angle\text{OHC} = 138^\circ$ . The question then arises whether the collinear  $^3\Pi$  interaction  $\text{O}(^3P) + \text{HF}$  is also unstable with respect to bending and whether a bent transition state is preferred for this reaction also. However, a major difference between the two reactions is that  $\text{O} + \text{HCl}$  is approximately thermoneutral whereas  $\text{O} + \text{HF}$  is endothermic by 34 kcal/mol.

The similarity in the  $\text{OH}^-$ ,  $\text{CH}_3\text{OH}^-$ , and  $\text{C}_2\text{H}_5\text{OH}^-$  spectra indicates that the pseudotriatomic model fairly successfully describes the polyatomic systems' spectra. However, development of theoretical methods of treating polyatomic reaction systems is clearly desirable. Further experiments from this laboratory will be forthcoming on transition-state spectra for tetraatomic systems, the results of which should be able to test theoretical methods for such systems.

**Acknowledgment.** Support from the Air Force Office of Scientific Research under Contract AFOSR-91-0084 is gratefully acknowledged. We thank Professor J. Wright for discussions on the rotated Morse potential surfaces. We thank the San Diego Supercomputer Center for a grant to undertake the ab initio calculations. S.E.B. acknowledges fellowship support from the University of California during the course of the research presented here.

**Registry No.**  $\text{H}_2$ , 1333-74-0; F, 14762-94-8; MeOH, 67-56-1; EtOH, 64-17-5;  $\text{OH}^\bullet$ , 3352-57-6;  $\text{MeOH}\cdot\text{F}^-$ , 80396-05-0;  $\text{EtOH}\cdot\text{F}^-$ , 135147-62-5;  $\text{OH}\cdot\text{F}^-$ , 36505-07-4.

(77) Schatz, G. C. *J. Phys. Chem.* **1990**, *94*, 6157.

(78) Rakestraw, D. J.; McKendrick, K. G.; Zare, R. N. *J. Chem. Phys.* **1987**, *87*, 7341.

(79) Gordon, M. S.; Baldrige, K. K.; Bernholdt, D. E.; Bartlett, R. J. *Chem. Phys. Lett.* **1989**, *158*, 189.

## Translational Energy Distribution from $\text{C}_2\text{H}_2 + h\nu(193.3 \text{ nm}) \rightarrow \text{C}_2\text{H} + \text{H}^\dagger$

J. Segall, Y. Wen, R. Lavi,<sup>†</sup> R. Singer, and C. Wittig\*

Department of Chemistry, University of Southern California, Los Angeles, California 90089-0482  
(Received: March 26, 1991)

We report the center-of-mass translational energy distribution for 193.3-nm photolysis of expansion-cooled  $\text{C}_2\text{H}_2$ , using high- $n$  Rydberg-level excitation of nascent H atoms to facilitate high-resolution time-of-flight measurements. The observed resolution of  $\sim 200 \text{ cm}^{-1}$  is presently limited by the ArF photolysis laser, whose band width is approximately  $200 \text{ cm}^{-1}$ . The reported distribution clearly resolves a  $\text{C}_2\text{H}$  bending progression ( $\nu_2 \sim 400 \text{ cm}^{-1}$ ), which reflects the trans-bent  $\text{C}_2\text{H}_2$  excited state. A definitive assignment of all features is still not possible on the basis of currently available information on  $\text{C}_2\text{H}$ . These measurements yield an upper bound to  $D_0$  of  $131.8 \pm 0.5 \text{ kcal mol}^{-1}$ .

### Introduction

The spectroscopy and photochemistry of acetylene have been studied extensively, both experimentally<sup>1-8</sup> and theoretically.<sup>9</sup> Early spectroscopic investigations showed a prominent bending progression in the  $\bar{A}^1A_u \leftarrow \bar{X}^1\Sigma_g^+$  absorption spectrum, indicating that the first electronically excited state is trans bent.<sup>1,2</sup> Photochemical studies showed that photolysis at wavelengths shorter than  $\sim 200 \text{ nm}$  yields the ethynyl radical,  $\text{C}_2\text{H}$ , and an H atom.<sup>3</sup> Wodtke and Lee reported the center-of-mass (CM) translational

energy distribution following 193.3-nm photolysis using the angle-resolved time-of-flight (TOF) method, and gave an upper

- (1) Innes, K. K. *J. Chem. Phys.* **1955**, *22*, 863.
- (2) Innes, K. K. *J. Chem. Phys.* **1955**, *22*, 863.
- (3) Irion, M. P.; Kompa, K. L. *Appl. Phys.* **1982**, *B27*, 183.
- (4) Wodtke, A. M.; Lee, Y. T. *J. Phys. Chem.* **1985**, *89*, 4744.
- (5) Ervin, K. M.; Gronert, S.; Barlow, S. E.; Gilles, M. K.; Harrison, A. G.; Bierbaum, V. M.; DePuy, C. H.; Lineberger, W. E.; Elisson, G. B. *J. Am. Chem. Soc.* **1990**, *112*, 5750.
- (6) Baldwin, D. P.; Buntine, M. A.; Chandler, D. W. *J. Chem. Phys.* **1990**, *93*, 6578.
- (7) Segall, J.; Lavi, R.; Wen, Y.; Wittig, C. *J. Phys. Chem.* **1989**, *93*, 7287.
- (8) Green, P. G.; Kinsey, J. L.; Field, R. W. *J. Chem. Phys.* **1989**, *91*, 5160.

\* Research supported by the U.S. Department of Energy under Contract DE-FG03-85ER13363.

<sup>†</sup> Present address: Soreq Nuclear Research Center, Yavne 70600, Israel.